Tampere University

Heidi Laitinen

HEAT TRANSFER SIMULATION OF STEEL CASTING PARTS' AIR QUENCHING PROCESS

Model improvement

Master's Thesis
Faculty of Engineering and Natural Sciences (ENS)
Examiners: University Lecturer Henrik Tolvanen
University Teacher Aleksi Sivonen
August 2023

ABSTRACT

Heidi Laitinen: Heat transfer simulation of steel casting parts' air quenching process
Master's Thesis
Tampere University
Master's Degree Programme in Mechanical Engineering
August 2023

Correct cooling rate in the quenching of steel casting parts is essential to achieve desired material properties. In this thesis, the heat transfer phenomena occurring during the air quenching process are examined, with the primary objective being on creating a coherent way of modeling this process with fluid dynamics software Ansys Fluent. This thesis is carried out as a customer project of Etteplan Oyj and is commissioned by Metso Oyj.

To achieve the objective of modeling the process consistently, literature research is conducted considering the phase transformations, external heat transfer mechanisms (convection and radiation) that occur during the quenching process, and the theory behind solving the fluid dynamics problem. This literature research forms the theoretical framework, which is the background for the development of a simulation procedure of heat transfer problem with the effect of phase transformations included. The cooling of steel casting parts is simulated in both forced and natural convection and compared to measured cooling data.

The achieved simulation results of both forced and natural convection cooling simulation correlate well with measured cooling data. Also the phase distributions acquired from the simulations are realistic. In the natural convection simulation, the effect of carbide formation and variation in grain size is taken into account. The uncertainties of the simulation are observed and explained, and possibilities on developing the air quenching simulation procedure further with regards to emissivity, fan modeling and calculation of the martensitic transformation constant are brought up.

Keywords: air quenching, heat transfer simulation, CFD

TIIVISTELMÄ

Heidi Laitinen: Teräsvaluosien ilmakarkaisuprosessin lämmönsiirtosimulaatio
Diplomityö
Tampereen yliopisto
Konetekniikan DI-ohjelma
Elokuu 2023

Teräsvaluosien karkaisussa tehokas jäähdytys on olennaista haluttujen materiaaliominaisuuksien saavuttamiseksi. Diplomityössä tutkittiin ilmakarkaisuprosessin aikana tapahtuvia lämmönsiirtoilmiöitä, ensisijaisena tavoitteena ollen luoda yhtenäinen tapa mallintaa prosessia Ansys Fluent -virtausdynamiikkaohjelmistolla. Diplomityö toteutettiin Etteplan Oyj:n asiakasprojektina Metso Oyj:n tilauksesta.

Ilmankarkaisuprosessin johdonmukaisen mallintamisen tausta-aineistoksi koottiin kattava kirjallisuustutkimus teräksen faasinmuutoksista, ulkoisista lämmönsiirtomekanismeista (konvektiosta ja säteilystä), jotka tapahtuvat karkaisuprosessin aikana, sekä virtausdynaamisen lämmönsiirtoongelman ratkaisemisesta laskennallisesti. Tämä kirjallisuustutkimus muodostaa teoreettisen viitekehyksen, joka on taustana ilmakarkaisuprosessin simulointimenetelmän kehittämiselle, jossa otetaan huomioon faasimuutosten vaikutus. Teräsvaluosien jäähtymistä simuloitiin tässä diplomityössä sekä pakotetussa että luonnollisessa konvektiossa ja verrattiin mittaustuloksiin.

Saadut simulointitulokset korreloivat hyvin mittaustulosten kanssa sekä pakotetun että luonnollisen konvektion simulaation osalta. Myös simulaatioiden antama faasijakauma on realistinen. Luonnollisen konvektion simulaatiossa karbidin muodostumisen ja raekoon vaihtelun vaikutus on otettu huomioon. Simulaatioiden epävarmuustekijöitä on havainnoitu ja selitetty ja lisäksi ilmakarkaisuprosessisimulaation kehittämismahdollisuuksia tuulettimen ja emissiviteetin mallintamiseen sekä martensiitin muodostumisvakion laskemiseen liittyen on tuotu esille tässä diplomityössä.

Avainsanat: ilmakarkaisu, lämmönsiirtosimulointi, CFD

PREFACE

This Master's thesis is carried out as a customer project of Etteplan Oyj, commissioned by Metso Oyj.

I would like to thank my supervisor Henrik Tolvanen from Tampere University for valuable feedback throughout this research and Henri Järvinen from Metso Oyj, who provided the basis and essential materials engineering expertise for this thesis. From Etteplan Oyj, I am appreciative of the support from Jani Sahramäki, whose earlier simulations on air quenching process were used as a starting point in the simulations of this thesis, and Matti Lindstedt for providing help with the CFD simulations and theory.

I would also like to thank my friends from Tampere University for making my student years truly memorable, my boyfriend for encouraging me during this process, and my family for all their support and encouragement throughout my educational journey.

In Tampere, 30th August 2023

Heidi Laitinen

CONTENTS

1. Introduction 1
2. Steel quenching process 3
2.1 Air quenching process of steel casting parts 3
2.2 Phase transformations during quenching process 4
3. Heat transfer in air quenching process 10
3.1 External heat transfer mechanisms 10
3.1.1 Forced convection 10
3.1.2 Natural convection 12
3.1.3 Radiation 12
3.2 Conduction 14
3.3 Modes of heat transfer during air quenching process 14
4. Simulation of heat transfer in air quenching process 16
4.1 Principle of Finite Volume Method 16
4.2 Governing equations 17
4.3 Turbulence models 18
4.4 Quenching process simulation in literature 21
5. Materials and methods 23
5.1 Research strategy 23
5.2 Air quenching process setup 24
5.3 Existing measurement data 26
5.4 Casting part phase transformation calculation 28
5.5 Simulation procedure 34
6. Results and discussion 40
6.1 Initial forced convection simulation 40
6.2 Improvements to forced convection simulation with solids-only model and full model simulation 42
6.3 Initial natural convection simulation 48
6.4 Inclusion of segregation by separated volume to natural convection simulation 51
6.5 Inclusion of segregation by modified starting time to natural convection simulation 53
6.6 Final forced and natural convection simulations with increased martensitic transformation start temperature 56
6.7 Key improvements of air quenching process modeling 62

7. Conclusions 65
References 67

SYMBOLS

Ae_1	lowest temperature to start austenitic phase transformation in equilibrium	K
Ae_3	equilibrium transformation temperature of completely austenitic microstructure	K
α	martensitic transformation constant	
α_r	surface absorptance	
α^*	coefficient damping the turbulent viscosity	
α_t	thermal diffusivity	m^2/s
β	thermal expansion coefficient	1/T
β_0	empirical coefficient for calculating the time of transformation of austenite	
B_s	highest temperature where bainitic transformation is possible	K
C_μ	function needed for calculating turbulent viscosity in realizable $k-\epsilon$ model	
C_{eq}	carbon equivalent content of the material	
c_p	specific heat	J/kgK
D	diameter	m
D_ω	cross-diffusion term for blending $k-\epsilon$ and $k-\omega$ models	
D_{eff}	effective diffusion coefficient	
δ_{ij}	Kronecker delta	
E_b	blackbody emissive power	W/m^2
ϵ	turbulence dissipation rate	m^2/s^3
ϵ_r	surface emissivity	
F_{ij}	view factor	
F_2	function needed for calculating turbulent viscosity in realizable $k-\omega$ model	
G	irradiosity	W/m^2
g	gravitation constant	m/s^2

G_{quantity}	generation term of quantity	
Gr	Grashof number, ratio of buoyant and viscous forces	
ΔH	enthalpy of transformation	J/m^3
h_0	enthalpy	J/mol
h_c	convection heat transfer coefficient	W/m^{2}K
J	radiosity	W/m^2
k	turbulence kinetic energy	J/kg
λ	thermal conductivity	W/mK
L_c	characteristic length	m
M_s	highest temperature where martensitic transformation is possible	K
μ	dynamic viscosity	kg/ms
μ_t	turbulent viscosity	kg/ms
N	grain size	
n	fraction of austenite transformed	
Nu	Nusselt number, dimensionless form of heat transfer coefficient	
ν	kinematic viscosity	m^2/s
ω	specific dissipation rate	m^2/s^3
p	pressure	Pa
Φ	dissipation function	
Pr	Prandtl number, ratio of kinematic viscosity to thermal diffusivity	
q	effective diffusion mechanism -dependent exponent	
$\dot{Q}_r$	net radiative energy exchange	W
$\dot{q}_c$	convective heat flux	W/m^2
$\dot{q}_r$	radiative heat flux	W/m^2
$\dot{Q}_v^{'''}$	rate of volumetric heat generation	W/m^3
Ra	Rayleigh number, characterizes a flow in natural convection	
Re	Reynolds number, used to determine whether flow is laminar or turbulent	
ρ	density	kg/m^3
ρ_r	reflection coefficient	
S_{ij}	mean strain rate	1/s
σ	Stefan-Boltzmann constant	5.67 $\times 10^{-8}$ Wm^{2}K^4

S_{quantity}	source of quantity	
$_B$	subindex, bainite	
$_F$	subindex, ferrite	
$_M$	subindex, martensite	
$_P$	subindex, pearlite	
τ	time of transformation	s
θ	angle of surface	rad
Θ_{ij}	visibility from surface i to surface j	
U	velocity	m/s
$u_{i/j/k}$	directional velocity	m/s
V	volume fraction	
w_{element}	percentage by weight	
x	coordinate at location	
y	distance to the next surface	m
Γ_{quantity}	effective diffusivity of quantity	
Y_{quantity}	dissipation of quantity	
y^*	dimensionless distance to the next surface	

TERMS AND ABBREVIATIONS

Ansys Fluent	fluid simulation software
ASTM	American Society for Testing and Materials
CCT-diagram	Continuous Cooling Transformation diagram
CFD	Computational Fluid Dynamics
FVM	Finite Volume Method
IT-diagram	Isothermal Transformation diagram
JMatPro	material properties software
RANS	Reynolds Averaged Navier-Stokes
S2S	surface-to-surface radiation model
TTT-diagram	Time-Temperature Transformation diagram

1. INTRODUCTION

Steel quenching is a process where a steel component is cooled from a high temperature to increase the hardness of the component. The hardening of the component is due to phase transformations. The rate of cooling affects whether a sufficient amount of the desired phases is formed, and is affected by the released heat from the phase transformations. Prediction of the effect on the cooling rate and the resulting phase composition is important. An accurate simulation is an effective way to predict whether the quenched component will achieve the needed phase composition as a result of cooling rate typically determined by the combination of cooling media and component geometry.

The aim of this thesis is to familiarize with the physics of the air quenching process and thus the first research question is to determine which phenomena have an effect on the process. Based on this research a coherent way to model air quenching of different steel compositions with a computational fluid dynamics (CFD) software is created. After finishing the research task of creating a consistent workflow for simulation, it is evaluated as the second research question how accurate are the results that can be achieved from the simulation with chosen way of modeling the process. This thesis is carried out as a customer project of Etteplan Oyj, commissioned by Metso Oyj.

The scope of this thesis is limited to the heat transfer process occurring during the quenching process. This means that despite the composition and phases of the steel used in simulations being investigated, the emphasis is on how they affect the cooling process. The phase changes affect the thermal conductivity and specific heat of the component and the heat released from the phase transformations slows the cooling. The quenching process has been studied with CFD in some studies, for example ones by J. Wang et al. (2008), Shang and Z. J. Wang (2010) and Xu et al. (2016). Most often the effect of phase transformations has not been taken into account.

The research questions and research task are

1. Question: Which phenomena have an effect on the air quenching process?

2. Task: What is a coherent way to model air quenching of different steel compositions?

3. Question: How accurate are the results that can be achieved from the simulation with the chosen way of modeling the process?

The method to answer the first research question, "Which phenomena have an effect on the air quenching process?", is literature research. The material for the research task of creating a coherent way to model air quenching of different steel compositions is acquired from the material properties software JMatPro, the measured data and the material acquired from the first research question. The second research question, "How accurate are the results that can be achieved from the simulation with the chosen way of modeling the process?", is answered based on results from the simulation results acquired from the research task.

The steel quenching process and the mathematical modeling of phase transformations are presented in chapter 2. The external heat transfer mechanisms are discussed in chapter 3, and in this chapter, it is also discussed how great an effect different mechanisms of heat transfer will have during the quenching process. The governing equations that are needed to solve the fluid dynamics problem and background of turbulence models and near-wall treatment methods used in this thesis are presented in chapter 4, which introduces the theory behind simulation of heat transfer during quenching process. In chapter 4, also examples of other studies considering the simulation of the quenching process are presented.

After the chapters that cover the theory behind the simulation, chapter 5 introduces the simulation cases and the strategy to solve them. Chapter 6 presents the results of the simulations and discusses how the simulation is improved along the way and what aspects affect the result. Lastly, in chapter 7, the results of the thesis are concluded and possibilities for further studies are presented.

2. STEEL QUENCHING PROCESS

Quenching is a heat treatment process used to increase the surface hardness by rapidly cooling a component from a high temperature, which causes phase transformations in the material. When quenching steel, the phase transformation that is generally desired to occur is one where austenite transforms into martensite. The illustrated example of rapid cooling where austenite transforms fully to martensite is presented in figure 2.1. The transformation is exothermic, so heat released during the transformation also affects the cooling process (Takeuchi and Yogo 2021).

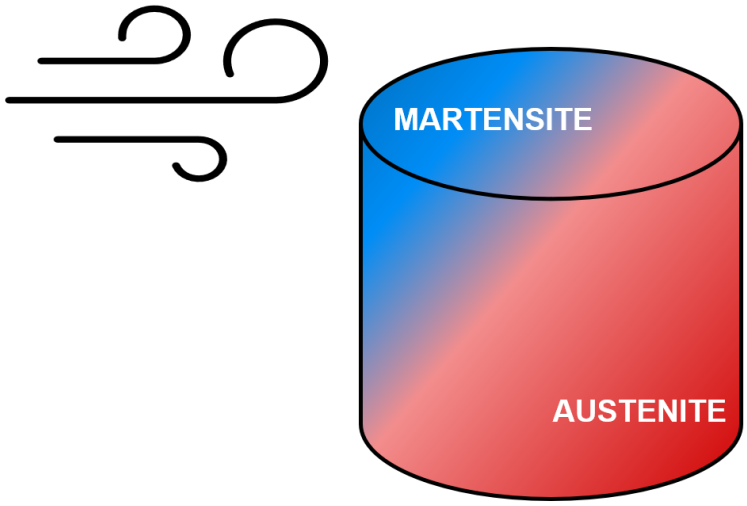

Figure 2.1. *Example of phase transformation from austenite to martensite due to rapid cooling.*

2.1 Air quenching process of steel casting parts

Quenching processes can be divided into liquid quenching and gas quenching. Liquid quenching consists of three stages, which are the vapor barrier formation stage, the vapor barrier collapse and the boiling stage and convection stage (MacKenzie 2005). The heat transfer rates vary remarkably between these three stages.

Gases, on the other hand, do not exhibit different cooling stages and heat transfer occurs by a convective heat transfer process. Gas quenching heat transfer process only happen-

ing in a single stage means that there are no radically different variations in temperature. Since the cooling rates are slower and more uniform in comparison to liquid quenching, distortion is reduced (Liscic et al. 2010, p. 445, 450).

Air quenching has many advantages besides low distortion, it has greater process flexibility to vary cooling rates and in comparison to oil quenching it is more environmentally friendly and does not produce toxic or combustible gases. The downside is that despite the possibility to increase the cooling rates by increasing the flow rate past the cooling metal surface, cooling is still insufficient to harden many steels (Liscic et al. 2010, p. 445). If mainly martensitic microstructure is desired from the quenching process, the size of metal components and species used is limited in comparison to oil or water quenching (J. Wang et al. 2008).

2.2 Phase transformations during quenching process

During the quenching process, the transformation from austenite to martensite is often desired to achieve a combination of high strength and satisfactory toughness. This requires a rapid enough cooling to avoid the formation of soft upper transformation products such as bainite, and in higher temperatures pearlite and ferrite, and to convert a sufficient amount of austenite to martensite. Bainite appears in an irregularly shaped lath- or plate-shaped form with carbide precipitation within the grains. The martensitic transformation is diffusion-less, due to which the composition of the martensite is the same as parent austenite (*ASM handbook. Volume 9, Metallography and microstructures* 2004, p. 166, 179).

Since the bainitic transformation occurs closest to the martensitic transformation, it is the one that often needs the most attention of the softer steel phases. The correct temperatures for each transformation can be estimated with a Time-Temperature Transformation (TTT) diagram, an example of which is illustrated in figure 2.2 (MacKenzie 2005). This diagram is also sometimes known as Isothermal Transformation (IT) diagram, since a way of obtaining the diagram for a particular steel is to heat a sample of steel to a high temperature, where it is completely transformed to austenite, and then transferred to a liquid bath of predetermined temperature. This way, the time it takes for the austenite to transform to another phase at a certain temperature can be determined, which gives the name for the Isothermal Transformation diagram. The TTT diagram can be built up by repeating this operation for different temperatures (Bolton 1994 - 1993, p. 238).

Determination of TTT diagrams for generalized use by experimental work only is impossible due to the wide alloy specification ranges, sharp sensitivity to composition changes and a dependency on grain size. For this reason, models have been developed to calculate these diagrams. The basis of the model of Kirkaldy and co-workers is clearly identifiable set of input parameters, so it is used in material properties software programs

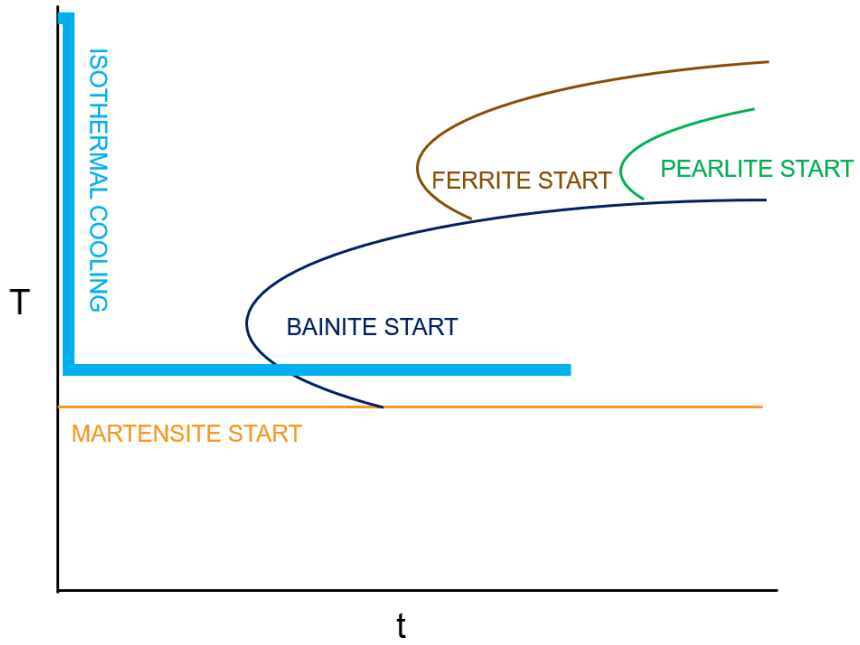

Figure 2.2. *Example of Time-Temperature-Transformation (TTT) diagram and "isothermal cooling" curve.*

such as JMatPro. The initial model solves the time τ it takes to transform n fraction of austenite at temperature T

$$\tau(n,T) = \frac{1}{\alpha_0(N)D_{eff}\Delta T^q}\int_0^n \frac{dn}{n^{2(1-n)/3}(1-n)^{2n/3}}, \tag{2.1}$$

where $\alpha_0(N) = \beta_0 2^{(N-1)/2}$, β_0 is an empirical coefficient, N is the ASTM (American Society for Testing and Materials) grain size, D_{eff} is an effective diffusion coefficient, ΔT is the undercooling with respect to the temperature below which the formation in question becomes thermodynamically possible (Ae_3, the equilibrium transformation temperature of completely austenitic microstructure, below which austenite is unstable with respect to ferrite, Ae_1, the lowest temperature to start austenitic phase transformation in equilibrium to pearlite or B_s, the starting temperature for bainitic transformation) and q is an effective diffusion mechanism -dependent exponent (Saunders et al. 2004).

The formula can be modified such that the only parameters that need to be determined are the grain size N, the composition of the material in wt% and the Ae_3, Ae_1 or B_s temperature of the material, which can be calculated as well. The modified equations for the time of transformation to ferrite (τ_F^{TTT}), pearlite (τ_P^{TTT}) and bainite (τ_B^{TTT}) are

$$\tau_F^{TTT}(n,T) = \frac{60w_{\text{Mn}} + 2w_{\text{Ni}} + 68w_{\text{Cr}} + 244w_{\text{Mo}}}{6\times 2^{N/8}\Delta T^3 D_F}\int_0^n \frac{dn}{n^{2(1-n)/3}(1-n)^{2n/3}}, \tag{2.2}$$

$$\tau_P^{TTT}(n,T) = \frac{1.8 + 5.4(w_{\mathrm{Cr}} + w_{\mathrm{Mo}} + 4w_{\mathrm{Mo}}w_{\mathrm{Ni}})}{6 \times 2^{N/8}\Delta T^q D_p} \int_0^n \frac{dn}{n^{2(1-n)/3}(1-n)^{2n/3}} \tag{2.3}$$

and

$$\tau_B^{TTT}(n,T) = \frac{(2.3 + 10w_{\mathrm{C}} + 4w_{\mathrm{Cr}} + 19w_{\mathrm{Mo}}) \times 10^{-4}}{6 \times 2^{N/8}\Delta T^2 \exp\left(-27500/RT\right)} \int_0^n \frac{dn}{n^{2(1-n)/3}(1-n)^{2n/3}}, \tag{2.4}$$

where D_F and D_P are

$$D_F = \exp\left(-23500/RT\right), \tag{2.5}$$

$$D_P = \left(\frac{1}{\exp\left(-27500/RT\right)} + \frac{0.5w_{\mathrm{Mo}}}{\exp\left(-37000/RT\right)}\right)^{-1} \tag{2.6}$$

and R is the gas constant. The value of q in equation 2.3 is composition dependent in the JMatPro program, becoming slightly lower than 3 with increasing levels of Cr, Mo and W. JMatPro system for solving the TTT diagrams has also more composition-dependent form of D_F and D_P and the volume fraction integral of time of transformation for bainite is also modified (Saunders et al. 2004). Inspection of equations 2.2, 2.3 and 2.4 shows that the results should be multiplied by 10^5 for realistic results.

If the phase transformation occurs with a constant cooling rate instead of constant temperature, Continuous Cooling Transformation (CCT) diagrams are used. An example of a CCT diagram and a cooling curve is illustrated in figure 2.3. The data from TTT diagram can be transformed to correspond to the values of the CCT diagram with the use of equation

$$\int_0^{\tau^{CCT}} \frac{dt}{\tau^{TTT}(n, T(t))} = 1 \tag{2.7}$$

(Lusk and Jou 1997). In practice, the phase transformation of the quenched component does not usually occur under the conditions of these diagrams, being cooled with constant cooling rate or held at a constant temperature.

The hardenability, which is often desired from the quenching process and is acquired through the martensitic phase transformation, can be increased further by increasing the alloying element content of the steel. Alloying elements, such as carbon, manganese, chromium and molybdenum cause a delay in transformation and thus reduce the critical cooling rate for martensitic transformation. Increasing the content of carbon and other alloying elements in the material has also disadvantages since this lowers the temperature at which the martensitic transformation M_s begins. Increasing the content of alloying elements also increases the distortion in the material and the possibility of cracking. The

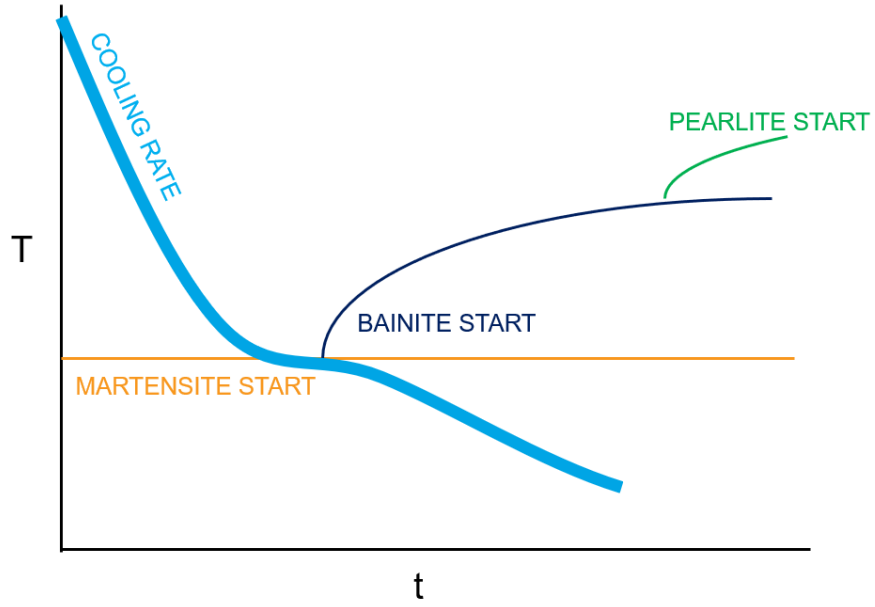

Figure 2.3. *Example of a Continuous Cooling Transformation diagram and an example of a cooling curve.*

"carbon equivalent" content of the material, that can be determined by

$$C_{eq} = w_{\mathrm{C}} + \frac{w_{\mathrm{Mn}}}{5} + \frac{w_{\mathrm{Mo}}}{5} + \frac{w_{\mathrm{Cr}}}{10} + \frac{w_{\mathrm{Ni}}}{10}, \tag{2.8}$$

where w_i is the weight percentage of an alloying element i. If the percentage of the "carbon equivalent" exceeds 0.52%, the material becomes prone to distortion and cracking (MacKenzie 2005). The composition of steel is not homogeneous, segregation of the alloying elements can cause local deviations to the material properties from the properties of the nominal steel composition (Hunkel 2021).

The determination of M_s temperature is an important aspect of martensitic transformation, especially if the material has a high content of alloying materials. Capdevila, Caballero, and Andrés (2002) used an artificial neural network to develop a widely applicable model to determine the M_s temperature based on the composition:

$$\begin{aligned} M_s/1[\mathrm{K}] =& 764.2 - 302.6w_{\mathrm{C}} - 30.6w_{\mathrm{Mn}} - 16.6w_{\mathrm{Ni}} - 8.9w_{\mathrm{Cr}} + 2.4w_{\mathrm{Mo}} - 11.3w_{\mathrm{Cu}} \\ &+ 8.58w_{\mathrm{Co}} + 7.4w_{\mathrm{w}} - 14.5w_{\mathrm{Si}}, \end{aligned} \tag{2.9}$$

where w_i is the weight percentage of component i in the material. For the start temperature of ferritic, pearlitic or bainitic transformation Ae_3, Ae_1 and B_s, there do not exist as widely applicable models, but correlations to use depend on the composition of the quenched material.

The volume fraction of martensite that forms can be estimated with modified Koistinen

and Marburger (1959) equation

$$V_M = (1 - V_B)[1 - \exp(-\alpha(M_s - T))], \tag{2.10}$$

where V_B is the volume fraction of bainite and α is the modification to the original equation, a constant depending on the composition of the steel. In the original equation, the parameter α was assumed to be independent of composition and to have the value of $\alpha = 0.011$ K^{-1} (Li et al. 2015). The determination of parameter α varies slightly depending on the source, for example, the correlation

$$\alpha/1[\mathrm{K}^{-1}]) = 0.0224 - 0.0107w_{\mathrm{C}} - 0.0007w_{\mathrm{Mn}} - 0.00005w_{\mathrm{Ni}} - 0.00012w_{\mathrm{Cr}} - 0.0001w_{\mathrm{Mo}} \tag{2.11}$$

by Bohemen and Sietsma (2009) is developed to predict the parameter α accurately for steels with a carbon content between 0.3 and 1.1 wt-%.

During the transformation process, the specific heat and thermal conductivity of the component change as a function of temperature and heat is released due to the exothermic transformation reaction (Takeuchi and Yogo 2021). Thermal conductivity and specific heat can be expected to be influenced significantly by the temperature and thermal history of the quenching process since a large number of microstructures with different compositions and distributions can be attained. At lower temperatures, there is a greater variation in thermal conductivity. (Peet, Hasan, and Bhadeshia 2011) Since the thermal conductivity and specific heat vary depending on the microstructure, conductivities for austenite, ferrite, pearlite, bainite and martensite need to be determined. The values for the specific heat and thermal conductivity can be found for example in *Heat Treating of Irons and Steels* by Dossett and Totten (2014) for some steels.

In addition to thermal conductivity and specific heat, another thing that needs to be taken into account is that the temperature is also affected by the transformation enthalpy, or latent heat released. When cooling down austenite, other phases, most often bainite, can also form alongside martensite so the enthalpy released from all phase transformations must also be taken into account. Figure 2.3 depicts the release of latent heat of martensitic transformation that causes the slowing of the cooling rate after the temperature is below the martensitic transformation starting point. The enthalpy of transformation from austenite to martensite is 6.400×10^8 J/m^3 according to Oliveira et al. (2010) and the initial used value for the simulation reported by Takeuchi and Yogo (2021). Other sources such as Denis, Farias, and Simon (1992) and Cheng et al. (2010) report similar values (6.48×10^8 J/m^3 and 6.28×10^8 J/m^3). There is slightly more variation between sources on the enthalpy of bainite transformation since Denis, Farias, and Simon (1992) report a value of 4.4×10^8 J/m^3 and Cheng et al. (2010) a value of 3.14×10^8 J/m^3, but neither of the sources consider the ferritic transformation. Oliveira et al. (2010) report a combined

value for both pearlitic and bainitic transformation as

$$\Delta H_{P,B}(^{\circ}\mathrm{C}) = 1.560 \times 10^{9} - 1.500 \times 10^{6} T \text{ [J/m}^3\text{]}, \tag{2.12}$$

where the amount of latent heat released is a function of temperature.

3. HEAT TRANSFER IN AIR QUENCHING PROCESS

3.1 External heat transfer mechanisms

Convection is one of three basic mechanisms of heat transfer, the others being conduction and radiation. When cooling a quenched product from a high temperature, there is heat transfer to the cooling fluid both by convection and radiation, so also radiation is studied in this section. Convection is heat transfer caused by the movement of a fluid, and it can be classified as forced or natural convection, depending on whether the fluid motion is initiated by external means or due to the difference in density of the fluid in different temperatures.

The rate of convection can be expressed by Newton's law of cooling:

$$\dot{q}_c = h_c(T_s - T_\infty), \tag{3.1}$$

where h_c (W/m^{2}K) is the convection heat transfer coefficient and T_s and T_∞ are the temperatures of the surface and the fluid far away from the surface. The dimensionless form of the heat transfer coefficient is the Nusselt number

$$Nu = \frac{h_c L_c}{\lambda}, \tag{3.2}$$

where L_c is the characteristic length and λ (W/mK) the thermal conductivity of the fluid (Mills 1999, p. 18, 255).

3.1.1 Forced convection

A feature of the flow that affects the convective heat transfer in forced flow is whether the flow is laminar with ordered flow motion or turbulent with disordered motion. Heat transfer by convection in turbulent flow is higher since the swirling eddies mix the fluid more effectively. Whether the flow is laminar or turbulent can be determined by the Reynolds number

$$Re = UL_c/\nu, \tag{3.3}$$

where U is the velocity of the fluid and ν (m^2/s) is the kinematic viscosity of the fluid. For a flat plate, the transition from laminar to turbulent flow is estimated to occur when $Re > 5\times 10^5$. Casted steel parts have irregular shape and rough surface which induce much earlier transition to turbulence.

When considering the development of heat transfer along a flat plate in a forced flow, the value for the heat transfer coefficient depends on the location along the plate. If the uniform forced flow hits the flat plate, the flow is at first laminar and the heat transfer coefficient decreases due to the boundary layer increasing. When the laminar boundary layer breaks into turbulent boundary layer, the value of the heat transfer coefficient swiftly increases during the transition (usually in the range $Re = 5\times10^4$–5×10^5) and then decreases with a less steep slope on the turbulent region (Mills 1999, p. 280, 281).

The laminar relation for a flow over a flat plate at location x can be solved from the energy equation to be

$$Nu_{x,lam} = \frac{h_{c,x}x}{\lambda} = 0.332Re_x^{1/2}Pr^{1/3}, \tag{3.4}$$

where Pr is the Prandtl number $Pr = \frac{\nu}{\alpha_t}$, where ν the kinematic viscosity and α_t (m^2/s) the thermal diffusivity. The equation holds when $Pr > 0.6$ and $Re_x < 5\times 10^5$. The relation for turbulent flow is acquired from experiments to be

$$Nu_{x,turb} = \frac{h_{c,x}x}{\lambda} = 0.0296Re_x^{0.8}Pr^{1/3}, \tag{3.5}$$

when $0.6 \leq Pr \leq 60$ and $5\times10^5 \leq Re_x \leq 10^7$ (Çengel 2015, p. 401–403, 428–249).

In practical applications other correlations can be more useful, such for surfaces with unheated starting section or uniform heat flux instead of uniform temperature (Çengel 2015, p. 430, 431). When considering a flow around a cylinder instead of a flat plate, the flow pattern depends very much on the Reynolds number. With low Reynolds number, the laminar flow either wraps around the cylinder or laminar vortices appear in the wake of the cylinder and at higher Reynolds numbers, the vortex street becomes turbulent or breaks down (Mills 1999, p. 284).

The relations for local values for the Nusselt number and the heat transfer coefficient are of limited value in heat transfer calculations since they require the average heat transfer coefficient. For equations 3.4 and 3.5, the average values can be achieved by integrating with respect to x. There are some experimentally determined average heat transfer coefficients for a flow over cylinders with different cross-sections and a sphere, such as the

relation from Churchill and Bernstein (1977) for Nusselt number is

$$\overline{Nu_{cyl}} = \frac{h_c D}{\lambda} = 0.3 + \frac{0.62 Re^{1/2} Pr^{1/3}}{[1 + (0.4/Pr)^{2/3}]^{1/4}} \left[1 + \left(\frac{Re}{282000} \right)^{5/8} \right]^{4/5}, \quad (3.6)$$

where D is the diameter. These relations only hold for specific types of flows. The relation 3.6 correlates well for experimental results when $RePr > 0.2$ (Çengel 2015, p. 440, 441). The magnitude of the average heat transfer coefficient in forced convection with the surrounding fluid being air should be between 10–200 W/m^{2}K (Mills 1999, p. 22).

3.1.2 Natural convection

The dimensionless number that characterizes a forced flow is the Reynolds number. For a natural flow, the Rayleigh number is the characteristic dimensionless number, and it can be calculated by

$$Ra_x = \frac{\beta \Delta T g x^3}{\nu \alpha_t}, \quad (3.7)$$

where β is the thermal expansion coefficient ($1/T$ for ideal gases), ΔT the temperature difference between surface and the ambient temperature, g the gravitation constant, x the characteristic length at the location. The transition to a turbulent flow occurs at a value $Ra_x \approx 10^9$. The Rayleigh number can also be described with Grashof and Prandtl number $Ra_x = Gr_x Pr_x$, where

$$Gr_x = \frac{\beta \Delta T g x^3}{\nu^2} \quad (3.8)$$

is the ratio of buoyant and viscous forces (Mills 1999, p. 293, 294).

Correlations for the Nusselt number of a vertical wall, horizontal cylinder, sphere and vertical wall are dependent on the Rayleigh number. There is also a correlation for the average Nusselt number of an arbitrarily shaped object, which is

$$\overline{Nu_{L_c}} = 0.52 Ra_{L_c}^{1/4} \quad (3.9)$$

where L_c is the characteristic length, or the length of the boundary layer. This correlation works when the Prandtl number for the fluid is not vastly smaller than 1 ($Pr \not\ll 1$). The magnitude of the average heat transfer coefficient in natural convection, where the surrounding fluid is air, should be between 3–25 W/m^{2}K (Mills 1999, p. 22, 295).

3.1.3 Radiation

When considering the heat transfer through radiation, two important terms are radiosity J (W/m^2), which describes the energy flux leaving the surface, and irradiosity G, which

describes the energy flux into the surface. For a black surface, which absorbs all incident radiation and does not reflect any, the radiation heat flux is given by Stefan-Boltzmann law

$$J = E_b = \sigma T^4, \tag{3.10}$$

where σ is the Stefan-Boltzmann constant equal to 5.67$\times$10^{-8} W/m^{2}K^4 and E_b is the blackbody emissive power. The heat flux due to radiation through a surface 1 to an enclosing surface 2 is

$$\dot{q}_{r1} = J_1 - G_1 = \epsilon_{r,1}\sigma T_1^4 - \alpha_{r2}\sigma T_2^4, \tag{3.11}$$

where ϵ_r is the emissivity and α_r is the absorptance of the surfaces (Mills 1999, p. 13–15).

If all the radiation from surface 1 is absorbed by enclosing surface 2 and $\epsilon_{r,1}A_1 \ll \epsilon_{r,2}A_2$ or $\epsilon_{r,2} \approx$1, the net energy exchange between the surfaces is

$$\dot{Q}_{r,12} = \epsilon_{r,1}A_1\sigma(T_1^4 - T_2^4). \tag{3.12}$$

This equation is useful in situations where a small object exists in large, nearly black surroundings (Mills 1999, p. 472).

There are several ways to model radiation, one being the surface-to-surface (S2S) radiation model, which can be used if the radiating surfaces can be assumed to be diffuse and gray and absorption and emission and scattering of the radiation can be ignored. The energy exchange between surfaces i and j depends on their size, distance from each other and orientation, which are accounted for by a view factor

$$F_{ij} = \frac{1}{A_i}\int_{A_i}\int_{A_j}\frac{\cos\theta_i \cos\theta_j}{\pi r^2}\Theta_{ij}dA_i dA_j, \tag{3.13}$$

where Θ_{ij} represents the visibility of surface dA_i to surface dA_j. The radiating flux out of the surface i can be written as

$$q_{out,i} = \epsilon_{r,i}\sigma T_i^4 + \rho_{r,i}\sum_{j=1}^{N} F_{ij}q_{out,j}, \tag{3.14}$$

where ρ_r is the reflection coefficient (Ansys, Inc. 2023a, p. 200, 201). For steels, the emissivity can vary remarkably depending on the composition, wavelength and temperature (Wen 2010).

3.2 Conduction

Convection and radiation are external heat transfer methods, whereas conduction is internal one. For metals and alloys, the heat is conducted by the movement of free atoms. In alloys, the movement of free atoms is restricted, which decreases the thermal conductivity λ (Mills 1999, p. 60). During the quenching process, the conductivity of the quenched component affects the process.

When the quenched component cools down, the temperature profile evolves determined by thermal conductivity and specific heat of the material and the heat generation in the component. Generally, both the thermal conductivity and specific heat of a phase increase with increasing temperature, and as the temperature differences during quenching process are large, it is important to take the temperature dependence into account.

According to the energy conservation principle, when studying the heat conduction inside a small volume in the quenched component of isotropic material, the energy balance can be written as

$$\rho c_p \frac{\partial T}{\partial t} = \frac{\partial}{\partial x_i}\left(\lambda \frac{\partial T}{\partial x_i}\right) + \frac{\partial}{\partial x_j}\left(\lambda \frac{\partial T}{\partial x_j}\right) + \frac{\partial}{\partial x_k}\left(\lambda \frac{\partial T}{\partial x_k}\right) + \dot{Q}_v^{'''}. \tag{3.15}$$

Here ρ is density, c_p specific heat and λ thermal conductivity of the material. The terms x_i, x_j and x_k are the coordinates in a three-dimensional heat transfer system. $\dot{Q}_v^{'''}$ is rate of volumetric heat generation (Mills 1999, p. 137). In the case of steel quenching, the volumetric heat generation is due to the phase transformations discussed in section 2.2. The phase transformations also affect the energy balance, since each phase has different values of thermal conductivity and specific heat, in addition to the temperature dependence of them.

3.3 Modes of heat transfer during air quenching process

The modes of heat transfer during quenching process are illustrated in figure 3.1. Alongside the external heat transfer modes, also the conduction affects during the air quenching process. The rate of conduction is material-dependent and changes as the austenite transforms to martensite and bainite, as was explained in chapter 2. The heat transfer though conduction is temperature-dependent and also depends on the phase transformations.

As can be seen from the equation 3.12, when the temperature of a small object is a lot greater than that of its surroundings, the heat transfer by radiation has a large effect on the total heat transfer from the object. When the temperature difference is small, so is the radiative heat transfer and its contribution to the total heat transfer. Equation 3.12 can

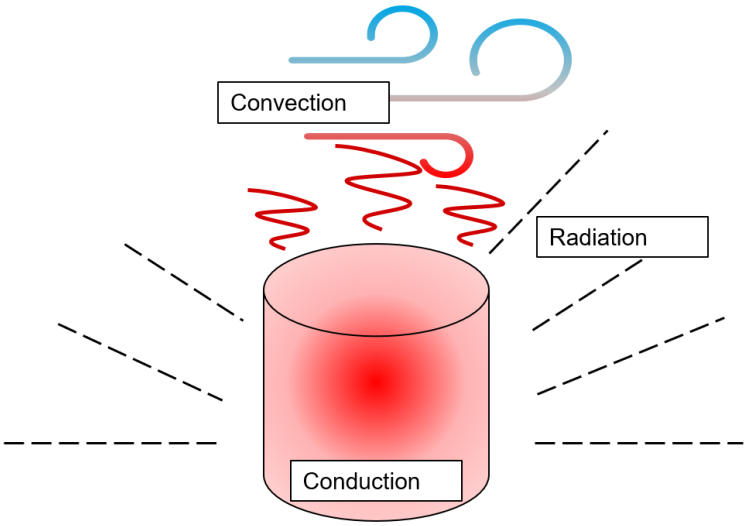

Figure 3.1. *Modes of heat transfer during air quenching process.*

be used to describe the radiation from the quenched component, since it is usually small compared to its surroundings and since the heat radiated by the quenched component is absorbed by the quenchant, the surroundings can be approximated as being black. It can be concluded that at the beginning of the quenching process when the quenched component is hundreds of degrees hotter than the quenchant, radiative heat transfer is important to take into account in calculations.

When the temperature of the quenched component starts to reach the temperature of the quenchant, convection has a bigger effect. The heat transfer rate is stronger in forced convection than in natural convection, as can be noticed from the magnitudes of the heat transfer coefficients in subsections 3.1.1 and 3.1.2. The quenching of the component is forced when the component is cooled with a fan, for example. When the heat transfer of the quenching is in question, the phase transformations end around 100 °C, so the radiation heat transfer will affect remarkably throughout the whole temperature scope that is of the most interest.

When studying the effect of external heat transfer mode during air quenching process, it needs to be noticed that the forced convection with high Reynolds number flow can bring some inaccuracy to the calculation. The flow pattern depends on the Reynolds number and, the turbulent flow is more complex. The form of the vortices and the flow is more dependent on the geometry, and as was discussed in subsection 3.1.1, the correlations for local Nusselt number are of limited value and only hold for specific types of flows.

4. SIMULATION OF HEAT TRANSFER IN AIR QUENCHING PROCESS

The heat transfer problem in the quenching process can be solved with computational fluid dynamics (CFD) solver that uses Finite Volume Method (FVM). This section discusses the governing equations and solution methods. It is also discussed how other authors have applied computational fluid dynamics when studying the quenching process.

The external heat transfer in the air quenching process, convection and radiation, is already introduced in chapter 3. The convection has an effect on the fluid patterns, as was discussed in chapter 3, so the modeling of turbulence and the fluid flow in CFD solvers is discussed more in-depth in sections 4.2 and 4.3. In the quenching process, the heat released from phase transformations needs to be taken into account. The equations for solving the amount of heat released are introduced in section 2.2.

4.1 Principle of Finite Volume Method

In order to solve the heat transfer problem with a CFD solver and Finite Volume Method, the geometry of the components and surroundings taking part in the heat transfer must be modeled. The geometry should be a simplified depiction of reality, but one which takes into account all the surrounding objects and shapes of components that have a significant effect on the heat transfer. The geometry is then divided into a mesh of smaller volumes (cells) and the heat transfer problem is solved for each of them.

The meshing, or the generation of the cells, has an effect on the quality of the simulation. The bigger the cells in the mesh are, the less accurate will the result be. The smaller the cells are, the more time-consuming the calculation will be. To balance between these two undesirables, the mesh is usually generated in a way that it is finer in areas of greatest interest or biggest changes in variables, and coarser where the gradients are smallest (Versteeg 2007, p. 2, 3). For example, the mesh should be finer in areas where the velocity gradients are steepest.

4.2 Governing equations

CFD solvers are algorithms that solve heat transfer or fluid flow problems by generating a mesh of the presented problem and solving the governing equations for each cell. The equations are continuity equation, momentum equation, energy equation and the equations of state (for pressure $p = p(\rho, T)$ and for enthalpy $h_0 = h_0(\rho, t)$). The continuity equation is

$$\frac{\partial \rho}{\partial t} + \text{div}(\rho u_i) = 0, \tag{4.1}$$

where the term $\frac{\partial \rho}{\partial t}$ describes the rate of change of the density, which for an incompressible fluid is 0, and the term $\text{div}(\rho u_i)$ describes the net convection of mass out of the element on each side of the element (Versteeg 2007, p.10, 24).

Momentum equation

$$\frac{\partial \rho u_i}{\partial t} + \text{div}(\rho u_i \times \ u_j) = -\frac{\partial p}{\partial x_i} + \text{div}(\mu \ \text{grad} \ u_i) + S_M \tag{4.2}$$

and energy equation

$$\frac{\partial \rho h_0}{\partial t} + \text{div}(\rho h_0 u_i) = -p \ \text{div} \ u_i + \text{div}(k \ \text{grad} \ T) + \Phi + S_{h_0} \tag{4.3}$$

are of a similar form. The first term on the left side of the equation describes the rate of change of velocity in equation 4.2 and of enthalpy h_0 in equation 4.3 of the fluid element and the second term describes the net rate of velocity in equation 4.2 and of enthalpy in equation 4.3 out of the element. On the right side of the equations, the divergence term is the diffusive term which describes the rate of change of velocity or enthalpy due to diffusion and S_M and S_{h_0} are the source terms of momentum and enthalpy depicting the rate of change of those two due to sources. The term k is the kinetic energy. The term Φ in equation 4.3 is the dissipation function, which includes the effect of the viscous stresses and is equal to

$$\begin{aligned} \Phi = \mu \Bigg\{ 2 \left[\left(\frac{\partial u_i}{\partial x_i} \right)^2 + \left(\frac{\partial u_j}{\partial x_j} \right)^2 + \left(\frac{\partial u_k}{\partial x_k} \right)^2 \right] + \left(\frac{\partial u_i}{\partial x_j} + \frac{\partial u_j}{\partial x_i} \right)^2 \\ + \left(\frac{\partial u_i}{\partial x_k} + \frac{\partial u_k}{\partial x_i} \right)^2 + \left(\frac{\partial u_j}{\partial x_k} + \frac{\partial u_k}{\partial x_j} \right)^2 - 2/3(\text{div} \ u_i)^2 \Bigg\}. \end{aligned} \tag{4.4}$$

The first term on the right side describes the effect of changes in pressure, or the normal stress (Versteeg 2007, p. 23, 24).

4.3 Turbulence models

As was discussed in chapter 3, at higher Reynolds numbers, the flows transition to turbulent. Laminar flows can be solved with equations 4.1, 4.2 and 4.3, but if the flow is turbulent, as in most engineering problems, the effects of turbulence need to be taken into account. Reynolds averaging is a method that approaches this problem by decomposing the turbulent velocity into the mean and fluctuating components $\overline{u_i}$ and u_i'

$$u_i = \overline{u_i} + u_i'. \tag{4.5}$$

A similar operation can be done for scalar quantities such as pressure and energy. Substituting the decomposed velocity into equations 4.1 and 4.2 yields the Reynolds-Averaged Navier-Stokes (RANS) equations

$$\frac{\partial \rho}{\partial t} + \text{div}(\rho \overline{u_i}) = 0 \tag{4.6}$$

and

$$\frac{\partial \rho \overline{u_i}}{\partial t} + \text{div}(\rho \overline{u_i} \times \overline{u_j}) = -\frac{\partial p}{\partial x_i} + \text{div}(\mu \text{ grad } \overline{u_i}) + \text{div}(-\rho \overline{u_i' \times u_j'}), \tag{4.7}$$

where Reynolds stresses $-\rho \overline{u_i' \times u_j'}$ need to be modeled to close equation 4.7 (Ansys, Inc. 2023a, p. 42).

A common approach to model the Reynolds stresses is to employ the Boussinesq hypothesis, which relates the Reynolds stresses to the mean velocity gradients

$$-\rho \overline{u_i' \times u_j'} = \mu_t \left(\frac{\partial u_i}{\partial x_j} + \frac{\partial u_j}{\partial x_i} \right) - \frac{2}{3} \left(\rho k + \mu_t \frac{\partial u_k}{\partial x_k} \right) \delta_{ij}, \tag{4.8}$$

where μ_t is turbulent viscosity, k turbulence kinetic energy and δ_{ij} Kronecker delta. This approach is used in the Spalart-Allmaras model, the $k-\epsilon$ models and the $k-\omega$ models. In the Spalart-Allmaras model, an additional transport equation needs to be solved for the turbulent viscosity. In $k-\omega$ models, additional equations for turbulence kinetic energy k and specific dissipation rate ω are solved. In $k-\epsilon$ models, the additional equations are for turbulence kinetic energy k and turbulence dissipation rate ϵ. The turbulent viscosity μ_t is computed as a function of k and ϵ or ω (Ansys, Inc. 2023a, p. 44).

There are three variations of $k-\epsilon$ turbulence model to be chosen in Ansys Fluent 2023 R1, the standard model, the RNG model and the realizable model, out of which the $k-\epsilon$ realizable model is recommended by *Ansys Fluent User's Guide* (Ansys, Inc. 2023b, p. 2007). The realizable model satisfies specific mathematical constraints on the Reynolds stresses that other models are unable, so it is presented below.

The modeled k and ϵ transport equations are

$$\frac{\partial}{\partial t}(\rho k) + \frac{\partial}{\partial x_j}(\rho k u_j) = \frac{\partial}{\partial x_j}\left[\left(\mu + \frac{\mu_t}{\sigma_k}\frac{\partial k}{\partial x_j}\right)\right] + G_k + G_b - \rho\epsilon - Y_M + S_k \tag{4.9}$$

and

$$\frac{\partial}{\partial t}(\rho \epsilon) + \frac{\partial}{\partial x_j}(\rho \epsilon u_j) = \frac{\partial}{\partial x_j}\left[\left(\mu + \frac{\mu_t}{\sigma_\epsilon}\frac{\partial \epsilon}{\partial x_j}\right)\right] + \rho C_1 S\epsilon + C_{1\epsilon}\frac{\epsilon}{k}C_{3\epsilon}G_b + S_\epsilon, \tag{4.10}$$

where $C_1 = \max\left[0.43, \frac{\eta}{\eta+5}\right]$, $\eta = S\frac{k}{\epsilon}$ and $S = \sqrt{2S_{ij}S_{ij}}$, where S_{ij} is the mean strain rate. G_k and G_b are representing the generation of turbulence kinetic energy due to mean velocity gradients and buoyancy, respectively. The effect of the fluctuating dilatation in compressible turbulence on the overall dissipation rate is represented by the term Y_M, and S_k and S_ϵ represent the source terms that the user can define. The terms C_2 and $C_{1\epsilon}$ are constants (C_2 = 1.9 and $C_{1\epsilon}$ = 1.44) and σ_k = 1.0 and σ_ϵ = 1.2 the turbulent Prandtl numbers for turbulence kinetic energy k and turbulence dissipation rate ϵ. The turbulent viscosity μ_t is calculated

$$\mu_t = \rho C_\mu \frac{k^2}{\epsilon}, \tag{4.11}$$

where the term C_μ is a function of the mean strain and rotation rates, the angular velocity of the system rotation and the k and ϵ turbulence fields (Ansys, Inc. 2023a, p. 55, 56).

The turbulence is affected by the presence of walls in simulation, so models for simulating the near-wall region are needed. The near-wall region can be divided into an almost laminar viscous sublayer, a fully turbulent layer and the blending region between them where the viscosity and turbulence both play equally important roles. The near-wall treatment methods that are considered in this thesis are Enhanced Wall Treatment, Menter-Lechner and Scalable Wall Functions (Ansys, Inc. 2023a, p. 133).

It is recommended that the $k-\epsilon$ model is used in combination with Enhanced Wall Treatment ϵ-equation or Menter-Lechner ϵ-equation (Ansys, Inc. 2023b, p. 2007). The Enhanced Wall Treatment divides the simulation domain into a fully turbulent region, which is solved using RANS model and a viscosity-affected region, which is solved using the Wolfstein model. The Wolfstein model solves the turbulent viscosity in the viscosity-affected regions by blending the fully turbulent formulation with the two-layer formulation of turbulent viscosity using a blending function. The law of the wall needs to be formulated as a single wall for the entire wall region despite the division into turbulent and viscous-affected regions, which is achieved by blending the laminar and logarithmic law-of-the wall using a blending function as well. The main idea of the Menter-Lecher is adding to the turbulence kinetic energy transport equation 4.9 a source term $S_{near-wall}$ that is only active in the

viscous sublayer and automatically becomes zero in the logarithmic region (Ansys, Inc. 2023a, p. 142–144, 148).

Another near-wall treatment besides Menter-Lecher and Enhanced Wall Treatment that is possible to use is Scalable Wall Functions with the assumption of fully turbulent flow, which is more independent from the quality of the mesh than the standard model since it uses grid refinement below the dimensionless wall distance y^* value of 11. A limiter is introduced for the y^* value so that the calculation always chooses the maximum of either y^* or
$y^*_{lim} = 11.225$ (Ansys, Inc. 2023a, p. 140). Because this wall treatment method gives is forgiving towards the quality of the mesh, it is also useful despite Ansys, Inc. (2023a) suggesting using the other near-wall treatments presented.

The $k-\omega$ models have some advantages in comparison to the $k-\epsilon$ model, the main one being that the ω-equation can be integrated without additional terms through the viscous sublayer. The recommended $k-\omega$ models are Baseline (BSL) and Shear-Stress Transport (SST), the latter of which is the turbulence default option in Ansys Fluent and can predict physical phenomena, such as separation, more accurately than $k-\epsilon$, but may be less stable and mesh-dependent in some cases (Ansys, Inc. 2023b, p. 2007, 2008).

The SST transport equations have the same form as the BSL

$$\frac{\partial}{\partial t}(\rho k) + \frac{\partial}{\partial x_i}(\rho k u_i) = \frac{\partial}{\partial x_j}\left(\Gamma_k \frac{\partial k}{\partial x_j}\right) + G_k + G_b - Y_k + S_k \tag{4.12}$$

and

$$\frac{\partial}{\partial t}(\rho \omega) + \frac{\partial}{\partial x_i}(\rho \omega u_i) = \frac{\partial}{\partial x_j}\left(\Gamma_\omega \frac{\partial \omega}{\partial x_j}\right) + G_\omega - Y_\omega + D_\omega + S_\omega + G_{\omega b}, \tag{4.13}$$

where G_k and G_ω represent the generation of k and ω, Γ_k and Γ_ω the effective diffusivity of k and ω and Y_k and Y_ω the dissipation due to turbulence. Terms S_k and S_ω are used-defined sources and G_b and $G_{\omega b}$ buoyancy terms. D_ω is the cross-diffusion term that blends the standard $k-\epsilon$ and $k-\omega$ models together. To account for the turbulent shear stress, the SST model calculates the turbulent viscosity by

$$\mu_t = \frac{\rho k}{\omega} \frac{1}{\max\left[\frac{1}{\alpha^*}, \frac{SF_2}{a_1 \omega}\right]}, \tag{4.14}$$

where S is the strain rate magnitude, α^* is a coefficient damping the turbulent viscosity, and F_2 is a function of k, ω, μ and the distance to the next surface y (Ansys, Inc. 2023a, p.61, 62, 68).

4.4 Quenching process simulation in literature

The quenching process has been simulated with CFD in some studies. J. Wang et al. (2008) simulated high-pressure gas quenching in their study "Numerical simulation of high pressure gas quenching of H13 steel" but did not take the phase transformations into account in their simulation. The equations in their simulation were solved with second-order upwind discretization for convection and SIMPLE algorithm for pressure-velocity coupling. The geometry of their simulation is a quenched cube in a cylindrical quenching chamber, where gas enters through circumferential nozzles. It is explained in the article of the study that the airflow is complex forced, turbulent flow, and standard $k - \epsilon$ turbulence model is chosen to be used in the simulation.

J. Wang et al. (2008) comment in their study that more accurate results than those in their simulation could be achieved if the phase transformations would have been taken into account since it is clearly seen when comparing the simulation results to the measurements that the formation of the bainite slows the cooling in the experimental result inside the cube. It is not stated whether the radiation is taken into account in the simulation, but due to the high initial temperature of the cube (1050 °C) it should have a remarkable effect on the cooling rate of the cube.

Shang and Z. J. Wang (2010) have similar geometry setup and the same models in their simulation, and they also have decided to ignore the latent heat release from the phase transformation. The experimental results seem to also be slightly slower, but since the quenching experiment in question is very quick, only lasting 680 s for the temperature to drop from 1503 K to 430 K, there is no bainite formation and the delay in the experimental results is explained by the gas charging time slowing down the beginning of the quenching. The error of their simulation in comparison to their measured data was 7.9 %.

The quenching simulation by Xu et al. (2016) takes into account the radiation by implementing the surface-to-surface (S2S) method in their simulation and Elkatatny et al. (2003) have chosen to use RNG $k - \epsilon$ turbulence model due to their complex geometry and high Reynolds number, but it seems that simulation of the latent heat from the phase transformations can be found more often in simulations made with Finite Element Method (FEM) solvers. For example S.-J. Lee and Y.-K. Lee (2008) have modeled the martensitic transformation using the modified version of the Koistinen-Marburger equation 2.10 and for ferritic, pearlitic and bainitic transformation they achieved the kinetic equations through optimization of the Kirkaldy equation 2.1. The cooling curve, phase fractions and distortions predicted by S.-J. Lee and Y.-K. Lee (2008) seem to correlate well with their measured data. Takeuchi and Yogo (2021) also used FEM software and took into account the latent heat of martensitic transformation, but achieved too large values for the total heat released in simulation where the value of latent heat is 80 kJ/kg.

In their study, Takeuchi and Yogo (2021) achieved more accurate results by halving the latent heat. They explained this with magnetic transformation since the latent heat due to phase transformation and magnetic transformation are not distinguished. In the case of a stress-induced martensitic transformation, magnetic transformation from paramagnetic austenite to ferromagnetic martensite can occur, but rapid increase of magnetization in case of plastic deformation seems to be linked with fracturing (Umakoshi and Yasuda 2011). The exact magnitude and effects of the magnetic transformation and its latent heat are not explained more in depth in the article by Takeuchi and Yogo (2021).

5. MATERIALS AND METHODS

5.1 Research strategy

In this thesis, the aim is to obtain a way to correctly model the quenching process involving phase transformations with CFD software Ansys Fluent 2023 R1. The main questions are modeling the convection and how to implement the latent heat from the phase transformations. An user-defined UDF code is written in Fluent to take into account the effect of phase changes. The mechanisms of phase transformation and heat transfer are studied through literature research and were discussed in chapters 2 and 3, and the theoretical background for the computational simulation of the quenching process is also considered through literature research in chapter 4.

The theory acquired through literature research in chapters 2, 3 and 4 is also applied in the simulation of the quenching process, which is discussed in sections 5.4 and 5.5. The simulation is made based on the measurement setup, and the results are compared to the measured cooling data of the setup. The workflow of the thesis, how different factors of it are connected and to which research question they answer is illustrated in figure 5.1. In figure 5.1, also different ways of implementing the formation of bainite that were considered in the process are presented alongside the reasons they are chosen not to be used.

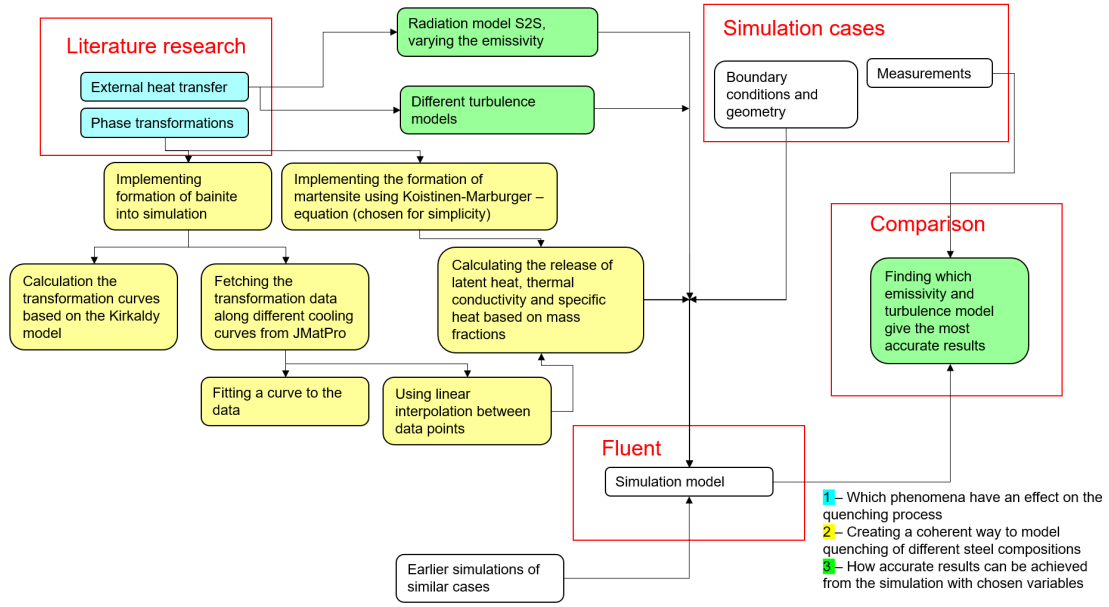

Figure 5.1. *Workflow of the thesis and to which research question which factor of the thesis answers.*

5.2 Air quenching process setup

In the modeled case the two quenched components of the same geometry exit a furnace on a furnace car having the simulation start temperature of 1020 °C. , A simplified version of them that is used in simulation is depicted in figure 5.2. The components are then quenched with a cooling fan in an industrial hall with an estimated ambient temperature of 30 °C. The length of the components is 750 mm, the thickness 120 mm, the width approximately 320 mm in the shorter end and 400 mm in the longer end. After studying the case with forced convection, the natural cooling of the components is studied. The measurements for the natural cooling were taken after the quenched components are split, so the length of the naturally cooled components is approximately 540 mm. The environment is otherwise similar as in forced cooling, only the fan is turned off.

The quenched components are held in their place on the furnace car by placing them symmetrically on a tray with pins attached to the tray holding the components still, all of which have an effect on the cooling of the components. The tray and the pins are approximated to be of general carbon steel, material properties of which are acquired from the Ansys Fluent material database to the simulation, the furnace car material is assumed to be concrete. The wall behind the furnace car is also expected to affect the simulation since the distance between the two is only 1.160 m. Distance to the wall where the furnace door is 1.050 m, so that wall is also expected to have an effect on the cooling airflow, but it is assumed that the furnace door is closed and insulated during the time of the cooling, so the temperature of the furnace is not influencing the cooling of the components after the furnace car exits the furnace.

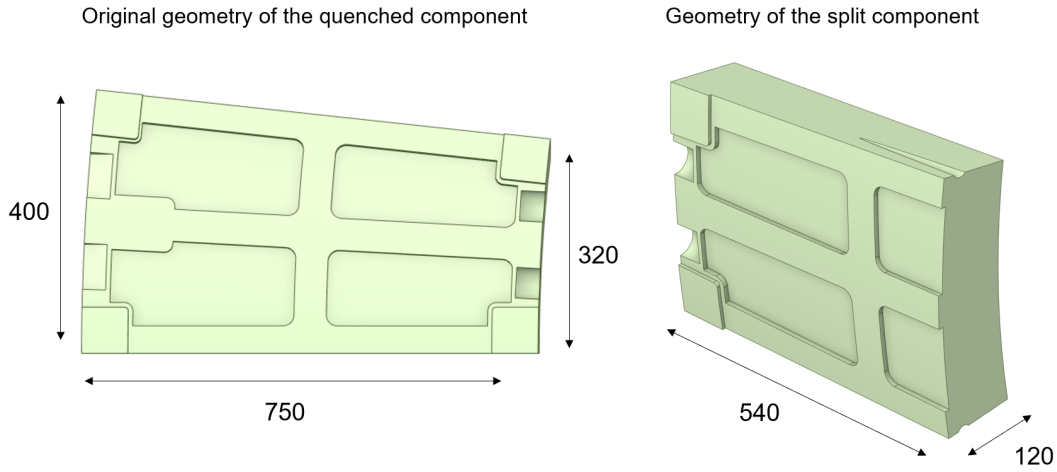

Figure 5.2. *Geometry of the quenched component before and after splitting.*

The maximum flow rate of air through the air-quenching fan is 50,413 m^3/h, and based on the blade angle of the fan, which is 30 °, the flow rate in the case of forced convection is 45,000 m^3/h. The distance from the floor to the midpoint of the fan is given to be 0.950 m. The distance between the fan and the furnace car is not given, but based on the photos of the quenching setup, it is estimated to be 2 m. The quenching setup is depicted in figure 5.3.

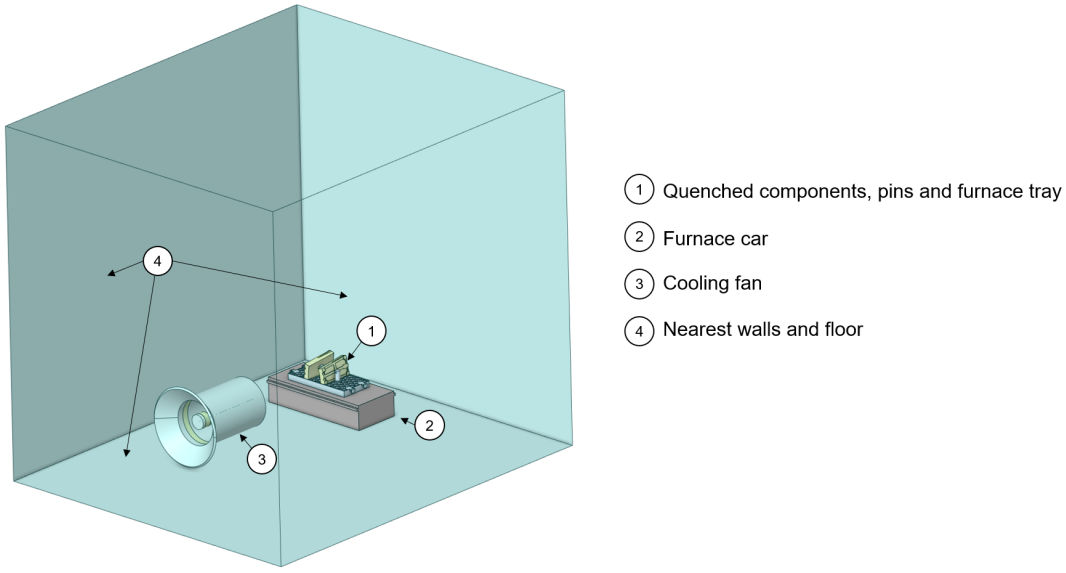

Figure 5.3. *The quenching setup.*

5.3 Existing measurement data

The material of the quenched component is H11-type steel. Based on the composition of the steel, the material properties are acquired from JMatPro software. The point where the measurements are taken is illustrated in figure 5.4. The measured forced cooling data, which is presented in figure 5.5 is from a component that exits at 1020 °C from the furnace. The component is measured 24 times, with the first measurement being taken after 1 minute of measured forced cooling, and the last one after 3.5 hours of cooling. The measurement after 1 hour was erroneously reported since the temperature at that point is reported to be 34 °C, so that measurement is left out of the analyzed data. The measurements were carried out by measuring three times the temperature in the middle of the component and marking the temperature as the average of these three measurements for each time point.

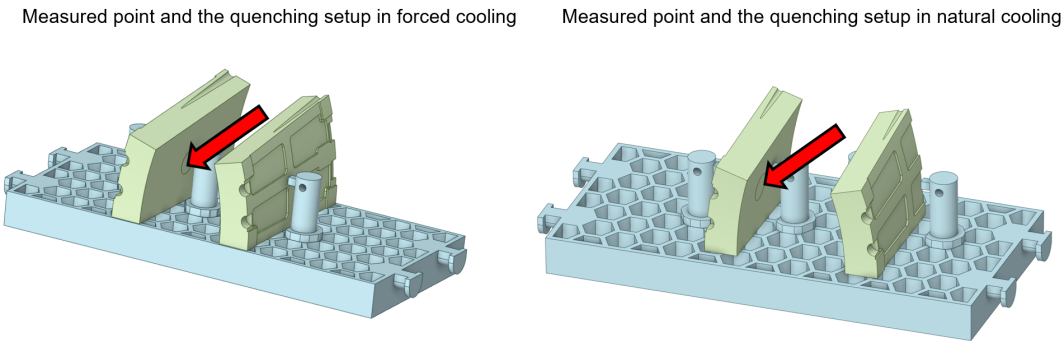

Figure 5.4. *Measured points in the cooling cases.*

In figures 5.5 and 5.6, the starting temperatures for bainitic and martensitic transformation are presented alongside the measured cooling, depicting the highest possible temperatures in which the transformation can occur. As can also be seen from figure 2.2, the martensitic transformation can be modeled as a straight line when simulating the phase transformations, but for the bainitic transformation the temperature changes depending on the time. From the figure 5.5, it is not clearly seen whether or not the cooling slows after the bainitic transformation start temperature is reached, so it can be approximated before simulation that there is not a great amount of latent heat being released due to the bainitic transformation in forced convection case.

From figure 5.6, it can be observed that the cooling slows down at a lot higher temperatures when the fan is not on and the convection is natural, close to the border where the bainitic transformation starts. It must also be noted that the time scale in figure 5.6 is over 4 times longer than in figure 5.5, up until 14.5 h, so the cooling is also initially a lot slower than in forced cooling. The reason for the temperature rise above the martensitic start temperature could be elemental segregation characteristic to large castings since

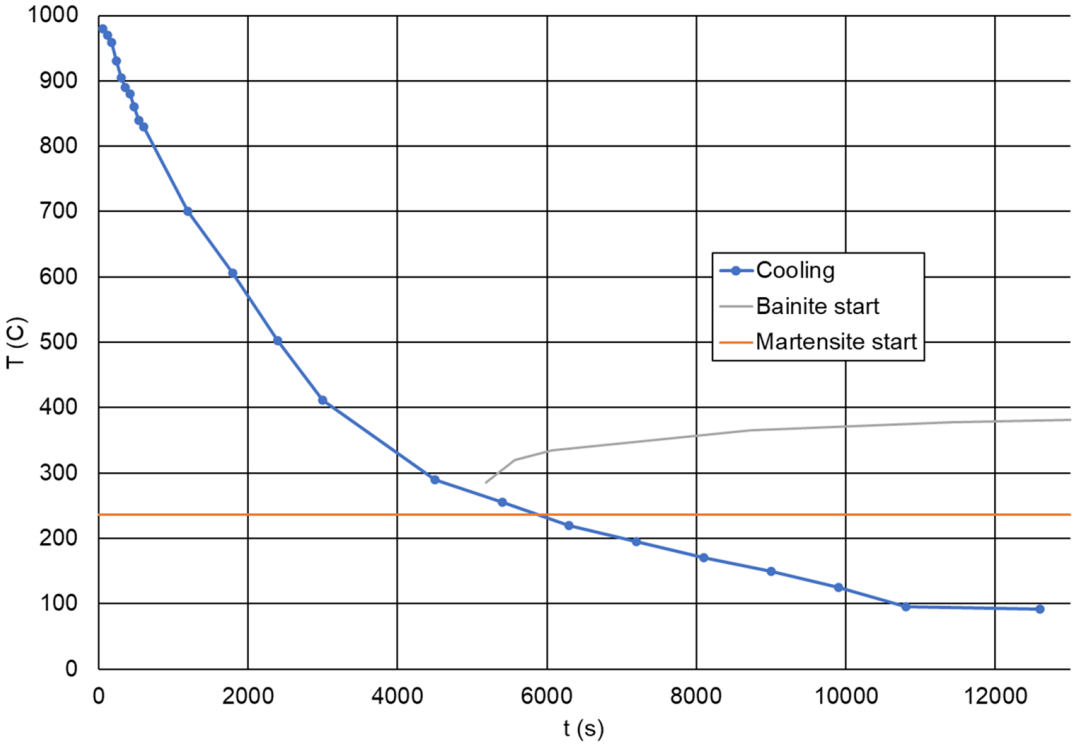

Figure 5.5. *The measured forced convection cooling data of the measured component and the start temperatures for bainitic and martensitic transformation.*

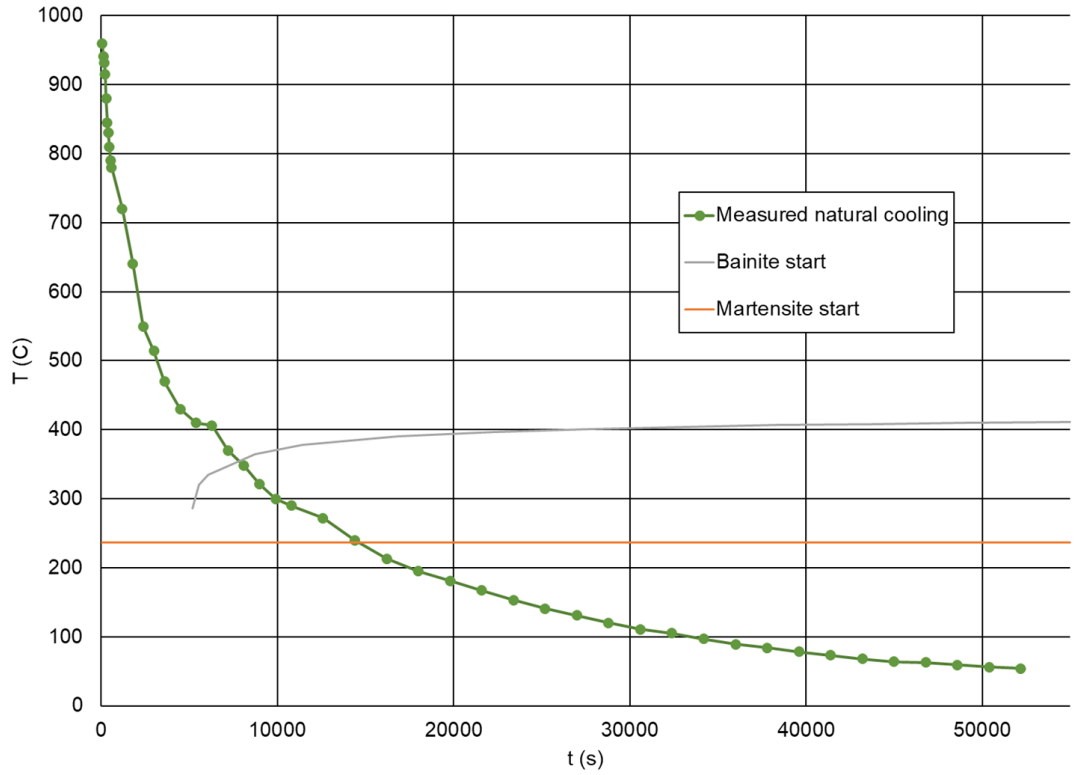

Figure 5.6. *The measured natural convection cooling data of the measured component and the start temperatures for bainitic and martensitic transformation.*

the chemical composition of the steel is not homogeneous in every part of the steel component, which may lead to a slight increase in transformation start temperatures in some parts of the component. This can lead, for example, to the unexpected formation of bainite in the regions containing less alloying elements. This could also be the reason why the cooling rate is slowing again slightly above the start of the martensitic transformation line.

5.4 Casting part phase transformation calculation

The simulation carried out in this thesis uses latent heat data obtained from JMatPro. The temperature-dependent latent heat release of the martensitic transformation was approximated from JMatPro data to follow the equation ([T] = K)

$$\Delta H_M \text{ [J/g]} = -9.48\times10^{-11}T^4+3.61\times10^{-8}T^3-3.27\times10^{-5}T^2+2.51\times10^{-2}T+99.04 \tag{5.1}$$

and for bainitic transformation

$$\Delta H_B \text{ [J/g]} = -2.05\times10^{-16}T^6+5.38\times10^{-13}T^5-6.69\times10^{-10}T^4+3.60\times10^{-7}T^3 \\ -1.30\times10^{-4}T^2+3.69\times10^{-2}T+157.85 \tag{5.2}$$

Another option would be to use the values for latent heat found in literature, for example, the ones that are presented in section 2.2, but these values for martensitic transformation are constants and for the bainitic they are either constants or linear functions, so the equations 5.1 and 5.2 are used. They differ considerably from the values provided by the literature, as can be seen from figure 5.7. The correlations used for latent heat in simulations are the ones acquired from JMatPro.

The thermal conductivity of the quenched component is also temperature-dependent. The coefficient for equations of thermal conductivity of austenite, bainite and martensite of form $\lambda = aT^3+bT^2+cT+D$ fitted to JMatPro data are presented in table 5.1. JMatPro also provides the effective thermal conductivity for the material for different cooling rates. The effective thermal conductivity for the forced convection cooling rate of the measured point seems to follow the fitted curve to austenite up until the start of martensitic formation at 503.15 K, so it can be expected also based on the thermal conductivity that not a lot of bainite will form during quenching since it does not affect the effective thermal conductivity remarkably.

The temperature-dependent correlations for the specific heat of a form $c_p = aT^6+bT^5+cT^4+dT^3+eT^2+fT+G$ are depicted in table 5.2. The correlations for thermal conductivity and specific heat for some steels can be found in literature, for example from *Heat Treating of Irons and Steels* by Dossett and Totten (2014), but the JMatPro library

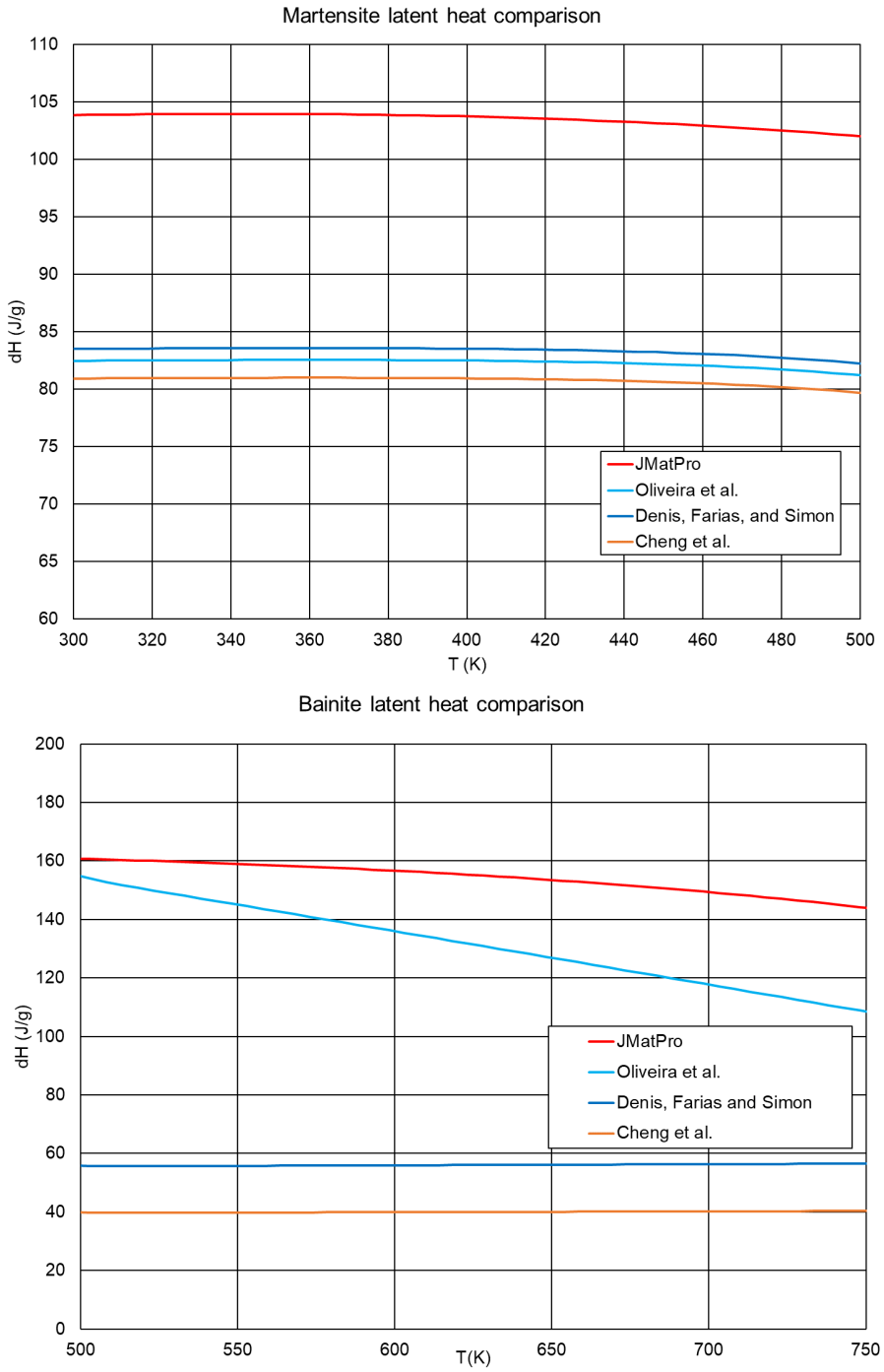

Figure 5.7. *Latent heat of martensitic and bainitic transformation provided by JMatPro compared to values reported in literature.*

is preferable since it holds information on these properties for a large variety of material compositions.

Different correlations hold for specific heat and thermal conductivity of different phases, which needs to be taken into account in the calculation. This has been implemented by calculating the value of each phase at each time step of the calculation. The effective values for specific heat and thermal conductivity are mass-weighted averages of these

[W/mK]	aT^3	bT^2	cT	D
λ_A		-3.94×10^{-8}	1.17×10^{-2}	13.64
λ_B	-4.92×10^{-8}	3.14×10^{-5}	2.62×10^{-2}	14.68
λ_M		1.44×10^{-5}	8.41×10^{-3}	14.30

Table 5.1. *Thermal conductivity of austenite, bainite and martensite of the quenched material.*

[J/gK]	$c_{p,A}$	$c_{p,B}$	$c_{p,M}$
aT^6	-3.69×10^{-19}		
bT^5	2.00×10^{-15}	3.43×10^{-15}	
cT^4	-4.47×10^{-12}	-9.44×10^{-12}	
dT^3	5.30×10^{-9}	1.11×10^{-8}	1.53×10^{-9}
eT^2	-3.55×10^{-6}	-6.41×10^{-6}	-1.86×10^{-6}
fT	1.44×10^{-3}	2.18×10^{-3}	1.15×10^{-3}
G	0.23	0.14	0.23

Table 5.2. *Specific heat of austenite, bainite and martensite of the quenched material.*

values for each phase. The correlations for thermal conductivity and specific heat represented in tables 5.1 and 5.2 are illustrated in figure 5.8

To calculate the masses of each phase at each time, information on the phase formation is needed. In this code, the data points for making the correlation of the bainite formation are collected from the JMatPro by keeping the cooling rate constant and tracking the volume fractions of the phases at each temperature at each point in time. This way of collecting the data was chosen since it gave the most data points, especially near the start temperature of martensitic transformation. JMatPro also has a possibility to generate the CCT diagrams for the chosen material, but this way the data points provided were a lot scarcer and did not provide data near the lower temperatures of bainite formation. The constant cooling rates should be chosen in a way that neither the slowest nor the quickest cooling rate of the component is outside the data to prevent erroneous interpolation, as is demonstrated in figure 5.9.

The data collected from JMatPro was used to bilinearly interpolate the mass fraction of bainite as a function of both time and temperature. Interpolated surface alongside the data points from JMatPro is illustrated in figure 5.10. This mass is then tracked at each time step of the simulation at each calculated point below the bainite formation starting temperature so that the mass of the bainite formed at the time step in question can be determined. The enthalpy of transformation of the newly formed bainite is released and the specific heat and thermal conductivity are recalculated based on the new composition of phases.

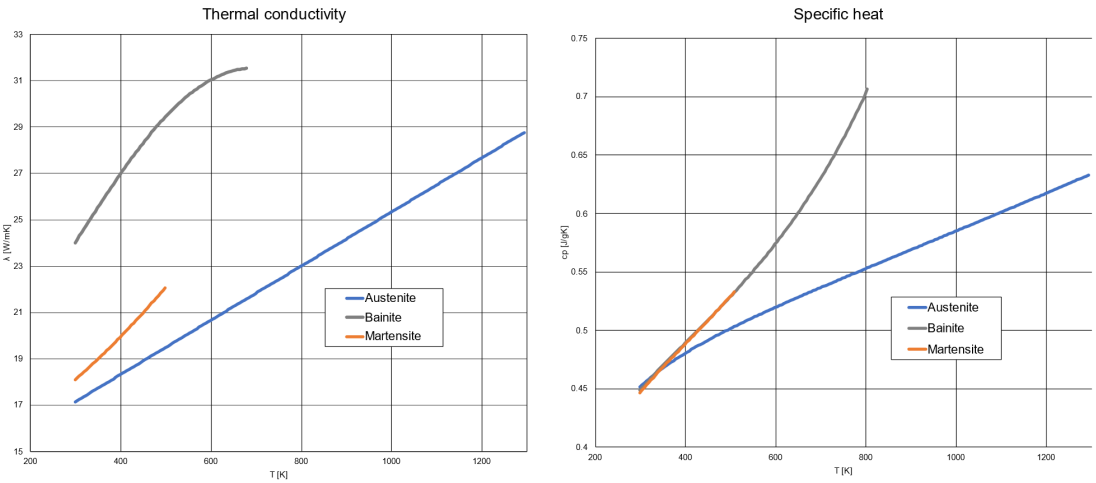

Figure 5.8. *Thermal conductivity and specific heat for austenite, bainite and martensite as a function of temperature for the material used in simulations.*

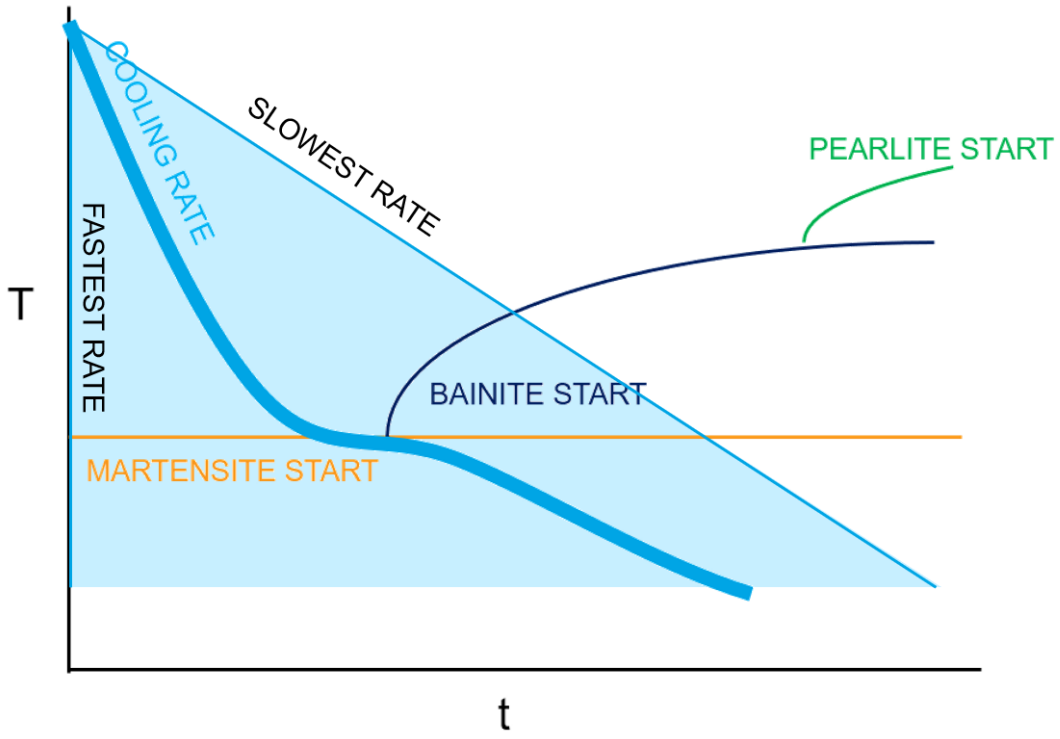

Figure 5.9. *An example of how the component cooling rate should be between the slowest and the fastest cooling rates acquired from JMatPro for the interpolation.*

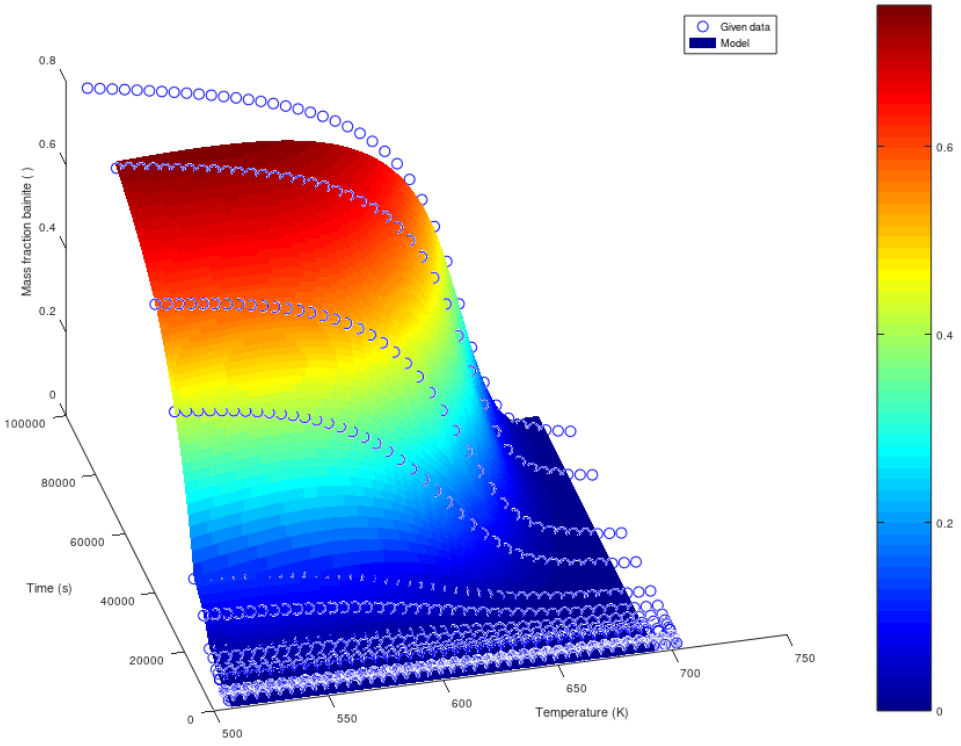

Figure 5.10. *Interpolated surface to find the bainite mass fractions and original data points.*

The formation of martensite is calculated by using equation 2.10. The parameter α for the steel used is calculated using equation 2.11 to equal 0.0168. It is also possible to use the data collected from JMatPro to fit a time-temperature correlation for martensite as was done for bainite, but the simpler method is chosen since equations 2.10 and 2.11 seem to predict the martensitic transformation quite well according to the literature. The equation also correlated well with the martensitic transformation data from JMatPro. The possibility of having a negative martensite formation rate due to possible temperature increase caused by the latent heat release of either martensitic or bainitic transformation is taken into account by checking whether the previous fraction is smaller than the current one. If that is the case, the current fraction of martensite is marked to be equal to the previous fraction. The formed fraction of martensite and bainite is subtracted from the austenite mass fraction.

If the temperature rises in the quenched component, this could cause a cell that already has martensite formed in it to return to the bainite formation area. For this reason, the code needs to check, how much bainite or martensite is already formed in the cell where transformations occur. Since temperature rises due to phase transformations, especially during natural convection, this could be the reason for simulation cases used as a starting point in this thesis cooling too slowly.

The formation of bainite could also be calculated without the data from JMatPro with the help of the TTT diagram equation 2.4. Using the TTT equation, the CCT diagram for the bainitic transformation can be calculated iteratively from equation 2.7. The correlation for the volume fraction of the bainite could then be found as a function of temperature and time by interpolating the mass fraction values between the data points from the achieved CCT diagram.

5.5 Simulation procedure

The simulations were carried out using fluid simulation software Ansys Fluent R1 2023. The simulated geometry was prepared with Ansys Spaceclaim R1 2023, based on the models and information on the quenching environment, which are described in section 5.2. As figure 5.11 illustrates, the real-world setup is used to create the CAD geometry for the simulation based on the initial data of the environment and the components. After the simulation case is defined in Fluent and initialized as the initial information suggests, the results of both forced and natural convection cases can be compared to the measurements. The mesh created from the CAD geometry has a surface mesh size of 15 mm on the surface of the components and 4 boundary layers from the surface with growth rate 1.2.

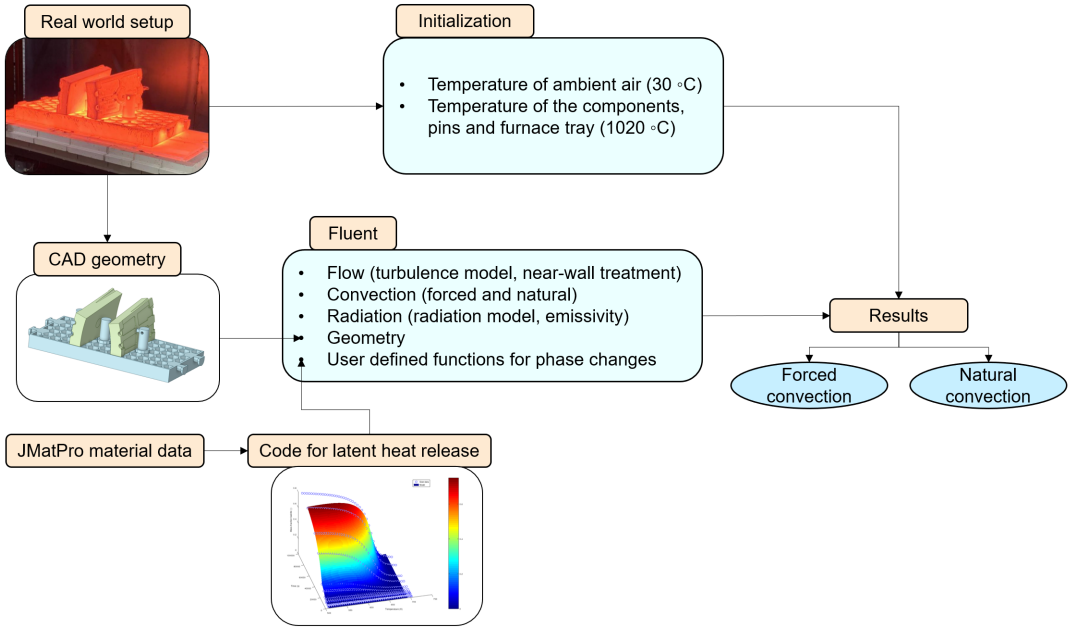

Figure 5.11. *Illustration of aspects that are taken into account to achieve simulation results from the real-world setup.*

The effect of phase changes is included with User Defined Functions, which are calculated as explained in section 5.4. The flow field is initialized for the forced cooling cases with steady-state solver and energy equation off and then switched to transient to simulate the cooling of the component with only the energy equation on and the flow field being frozen to the one acquired from steady-state simulation. The simulations are carried out this way to reach reasonable simulation times. The radiation model that is used in the calculations is the surface-to-surface (S2S) model, the theory of which is presented in subsection 3.1.3, with temperature-independent emittance assumed. The fan is simulated as a 3D zone, so a volume inside the fan is assigned to apply a momentum source.

In Fluent, the 3D fan model simulates the effect of an axial fan. The swirl velocity, fan origin location, hub and tip radius, thickness of the fan and inflection point (the fraction

of the blade length over which the tangential velocity of the fan discharge increases with increasing radius) of the blade need to be determined. As was discussed earlier in section 5.2, the fan geometry and location are approximated, so this can be a cause of slight inaccuracy. The inflection point of the blade is also assumed to be the default value 0.83, since the blade geometry is not available, and the pressure jump assigned to the fan zone is constant and not a function of flow rate. These simplifications can cause inaccuracy in comparison to reality.

Figure 5.12 shows the steps taken to develop a systematic workflow to model air quenching process. The differences and reasons for conducting each simulation are explained in this section. Each simulation is modified based on the observation made from earlier simulations, the results of which are discussed in chapter 6.

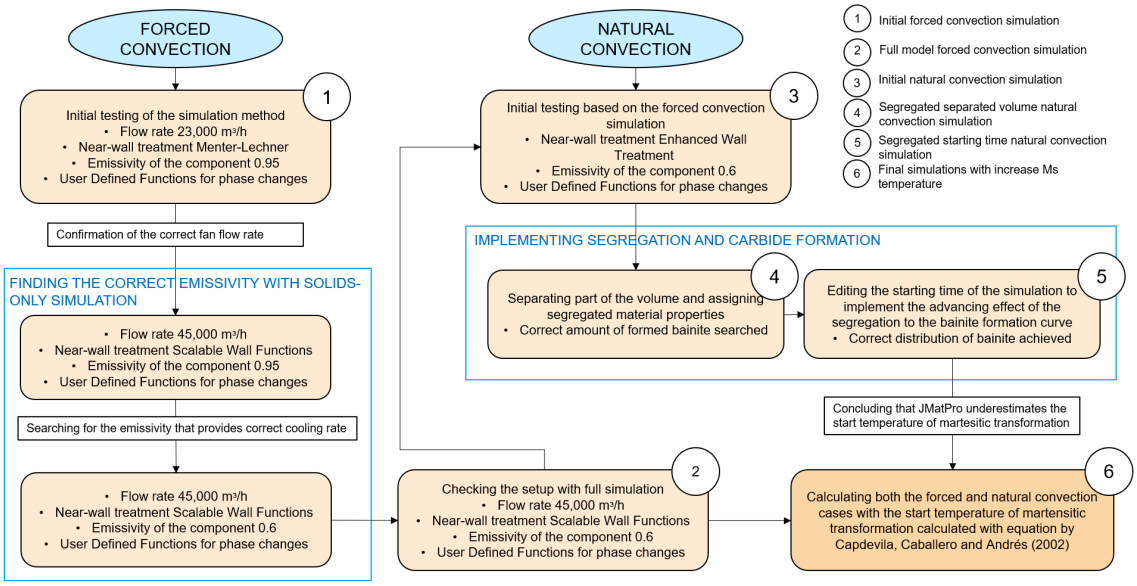

Figure 5.12. *Simulations carried out in this thesis.*

The mass fractions of formed phases in each simulation are studied. The mass fractions are illustrated on two surfaces inside the component, that are in the same location in each simulation. The cross-sections from the middle of the quenched component, cut in both longitudinal and latitudinal directions, which show the mass fraction of each phase inside the component are illustrated in figure 5.13.

The simulation of the quenching process in this thesis uses earlier simulation cases on the same subject carried out by Etteplan Oyj as a starting point, alongside the literature research on the theory. Earlier simulations have struggled with unrealistically slow cooling in comparison to measured results, which has led to the simulations predicting erroneous amounts of the steel phases in the end result. The hypothesis of why earlier simulations failed to cool as fast as the measurement is that the phase transformations modeling is incorrect in a way that too much of the latent heat is released. The reason for this might be that the possibility of a single cell starting to form bainite due to heating up after partially

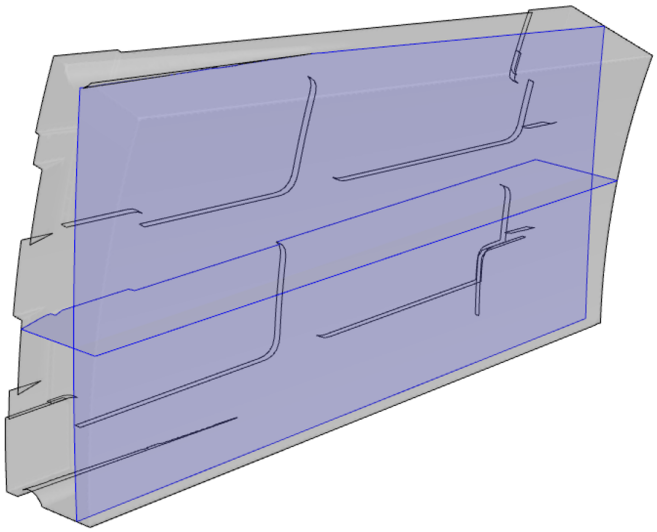

Figure 5.13. *Surfaces where the mass fractions of each phase are taken.*

transforming to martensite is not taken into account, and thus too much of the bainite is forming. The data about bainitic transformation was scarcer in the earlier simulations, which also may have an effect on the simulation.

Initially, the simulation (Initial forced convection simulation) studies only the forced convection case and is carried out with realizable $k - \epsilon$ model with Menter-Lechner wall treatment and internal emissivity of 0.95, as this combination was used also in earlier simulations of a similar sort. The fan is simulated as a 3D fan zone, which produces a volume flow of 22,810 m^3/h as an initial guess since the correct flow rate is not yet known in this simulation. This flow is smaller than is reported in section 5.2 since the rate of the actual airflow was acquired only later on. The main reason to conduct this simulation is just to ensure the accuracy of the code calculating the phase transformations. The formation of bainite and martensite seems to work accurately, so the fault of the earlier simulations has been fixed in the current code. The cooling seems to be quicker than in the measurement data, despite the volume flow being smaller than reported, and slower after the beginning of the martensitic transformation. The results of this simulation are analyzed more in-depth in section 6.1.

In section 6.2 (Improvements to forced convection simulation with solids-only model and full model simulation), improvements are made with the aim is to find the correct emissivity and flow rate for the correct cooling rate before the phase transformations for the forced convection case. The wall functions are changed to Scalable Wall Functions since they should provide more accurate results even if the mesh is not fine enough near walls. The correct cooling rate is provided by the manufacturer in this simulation to be 45,000 m^3/h. To find the correct emissivity effectively, the heat transfer coefficient and view factors on the walls of the solids are calculated with a fluid-only model, and then the cooling is simulated with a solids-only model. Since only the energy equation needs to be solved

in a solids-only model, the solver process can be executed with a much larger time step (60 s) than in the earlier simulation, where the time step was 1 s. But, since the heat transfer will not be simulated correctly with this type of model, after finding the proper value for the emissivity quickly, the case is then simulated again with both the fluid and the solid participating in the calculation similarly as in the initial simulation, the flow field being frozen to the one acquired from a steady-state simulation.

Section 6.3 (Initial natural convection simulation) focuses on the natural convection case. This case is expected to produce more bainite than the case with forced convection since the temperature is within the bainite formation range much longer than when the fan is cooling the components. Since the flow caused by the temperature differences in the air is laminar in a large part of the analyzed area, the wall treatment method is switched from Scalable Wall Functions, which assume fully turbulent flow, to Enhanced Wall Treatment. The simulation is carried out with all the equations on, so the flow is not frozen at any point. Natural convection cannot be simulated with the flow frozen since it depends on the surface temperature and changes as the component cools down. Due to the flow of the fluid in natural convection being a lot smaller than in forced convection, this allows a bigger time step (up to 20 s) for the flow than the forced convection case would. Therefore, the length of the calculation is in a reasonable range to carry this simulation out with the flow on.

Based on the results of the initial natural convection simulation, it is concluded that the effect of elemental segregation in the heat-treated casting (annealing carried out at 1020 °C) should be investigated. According to earlier measurements, it is noticed that this type of steel is largely heterogeneous in terms of the carbon concentration inside the component. In segregated areas, the concentration of the alloying component is larger than in the original composition. In figure 5.14, the lighter areas and darker areas inside them are of a segregated composition and the dark, ribbon-like areas surrounding them are carbides. As can be seen from the figure, the grain size can also vary a lot in component, which moves the start of the bainitic transformation curve earlier in time.

It should be noticed that the material in figure 5.14 is the result of cooling with forced convection. When cooling with natural convection, it is likely that a significant amount of carbides will form approximately between temperatures 1000 °C and 900 °C. n areas with a lot of formed carbides, the surrounding matrix contains significantly less carbon and alloying elements. JMatPro does not consider the possibility of high-temperature carbide formation in this material as with the nominal chemistry the driving force for carbide formation is much smaller compared to segregated microstructure corresponding much better with the reality. This leads to a rise in the starting temperatures of martensitic and bainitic transformation, which explains why the cooling curve in the initial natural convection simulation is not correct near the bainitic and martensitic transformation start temperatures.

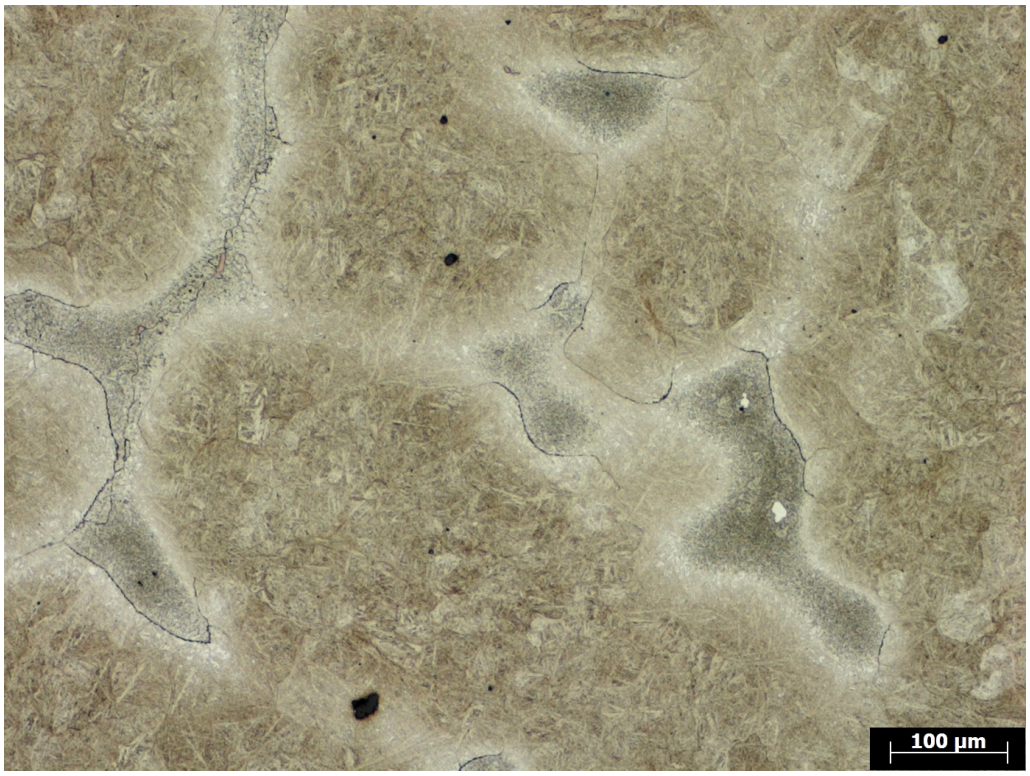

Figure 5.14. *Segregated, lighter and darker areas and varying grain sizes in material cooled with forced convection and formed carbides in dark, ribbon-like areas near the segregated areas. Image provided by Metso Oyj.*

In section 6.4 (Inclusion of segregation by separated volume to natural convection simulation), the segregation and different grain size are taken into account by splitting the components into two volumes, the surface volume 10 mm from the surface, which is around 15% of the total volume, and the inner volume. The material properties of the inner volume follow the properties retrieved from JMatPro based on the material composition reported, but the properties of the segregated surface volume are retrieved with 75% carbon concentration and grain size reduced to a fifth of the original. The martensitic transformation start temperature in the surface volume is 271.7 °C and the highest bainitic transformation start temperature is 456.8 °C.

The composition with 75% of the original steel concentration did provide a result that confirmed the need for including the segregation for the simulation to be able to follow the measured cooling curve. The results still showed that the amount of bainite forming in the segregated volume extracted up to 10 mm from the surface was not big enough to contribute a correct amount of released heat from bainitic transformation. To find the correct amount of formed bainite, a bigger amount of the volume was extracted to the segregated volume, up to 20 mm from the surface. This segregated surface volume is around 33% of the total volume and produced the desired amount of heat from the bainitic transformation.

Since the segregated areas are distributed in the entire volume of the casting, the correct distribution of formed bainite and martensite cannot be achieved by assigning the segregated material properties to specific areas. Since the main issue with the original material composition is that considerably less bainite is formed than should have been based on the latent heat that should have been released, it is estimated that in natural convection simulation, the main cause of the error is that the formation of carbides is not taken into account, and due to this, the original bainitic transformation curve is not suitable to reflect the real bainitic transformation curve of the components in natural cooling. The start time of the bainite transformation must be moved to an earlier time by modifying the starting time of the simulation to be 20,000 s in simulation 6.5 (Inclusion of segregation by modified starting time to natural convection simulation), so when the component reaches suitable bainitic transformation temperature, a more accurate amount of bainite will form.

The starting temperature of the martensitic transformation seems to be systematically underestimated by JMatPro software, as can be noticed from the simulations conducted. For the final simulation in section 6.6 (Final forced and natural convection simulations with increased martensitic transformation start temperature) both the forced convection and natural convection are simulated with the starting temperature of martensitic transformation calculated with equation 2.9 by Capdevila, Caballero, and Andrés (2002). The resulting martensitic start temperature is 293.9 °C, which probably overestimates the start temperature of the nominal composition, but seems to be very accurate in the natural convection case due to the effect of segregation. Also the differences between the frozen and non-frozen flow fields are investigated, with the non-frozen flow started with 1 s time-step and raised to 10 s.

6. RESULTS AND DISCUSSION

6.1 Initial forced convection simulation

The main reason for conducting this simulation was to ensure the accuracy of the code calculating the phase transformations since more accurate data on the cooling fan was received later. The resulting cooling curve of the initial forced convection simulation at the same point as the measurements were taken is shown in figure 6.1 alongside the measured cooling. The start temperature of the martensitic transformation is depicted in figure as well, to clarify that it is indeed due to the martensitic transformation that the cooling of the component slows down remarkably around 237 °C.

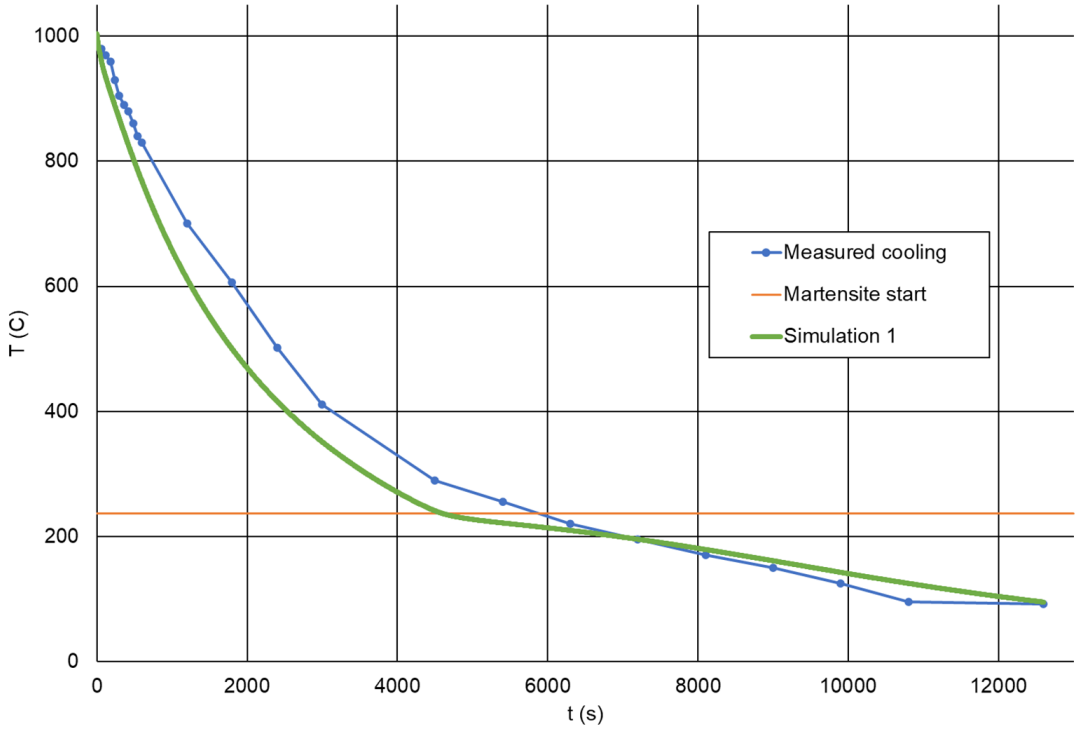

Figure 6.1. *Cooling rate of the initial forced convection simulation compared to the measured cooling rate with marked start temperature of martensitic formation, time step size 1 s.*

As can be seen from figure 6.1, at the temperature where the martensitic transformation starts, the simulated cooling slower than measured. The latent heat released from

the martensitic transformation at the martensitic start temperature seems to have greater value than in reality, the reason of which could be that the latent heat of the magnetic transformation is not taken into account, as Takeuchi and Yogo (2021) have also concluded in their study. A more likely scenario is that in the current simulation, the transformation from austenite is occurring at a lower temperature than in the measured case since at lower temperatures the cooling effect especially through radiation will be smaller. The assumption of too large latent heat release could also be due to the martensite forming initially too fast, due to the martensitic transformation constant being too big.

The mass fractions of formed martensite and bainite and the amount of austenite left after 3.5 h of cooling are presented in figure 6.2. Based on the distribution of each phase and the slowing effect the martensitic transformation has on the cooling curve in figure 6.1, the code computing phase transformation seems to be working accurately. Since the amounts of each phase are very different from each other, it needs to be noticed that the scales on each sub-figure are different.

It can be assumed that the amount of bainite that forms in this simulation is less than in the measured case since the quicker the cooling, the less bainite can form. As can be seen from figure 6.1, the simulated cooling is faster than the measured cooling. The average austenite mass fraction that is left at the end of the simulation is 0.089, and the maximum temperature of the components is 117.15 °C.

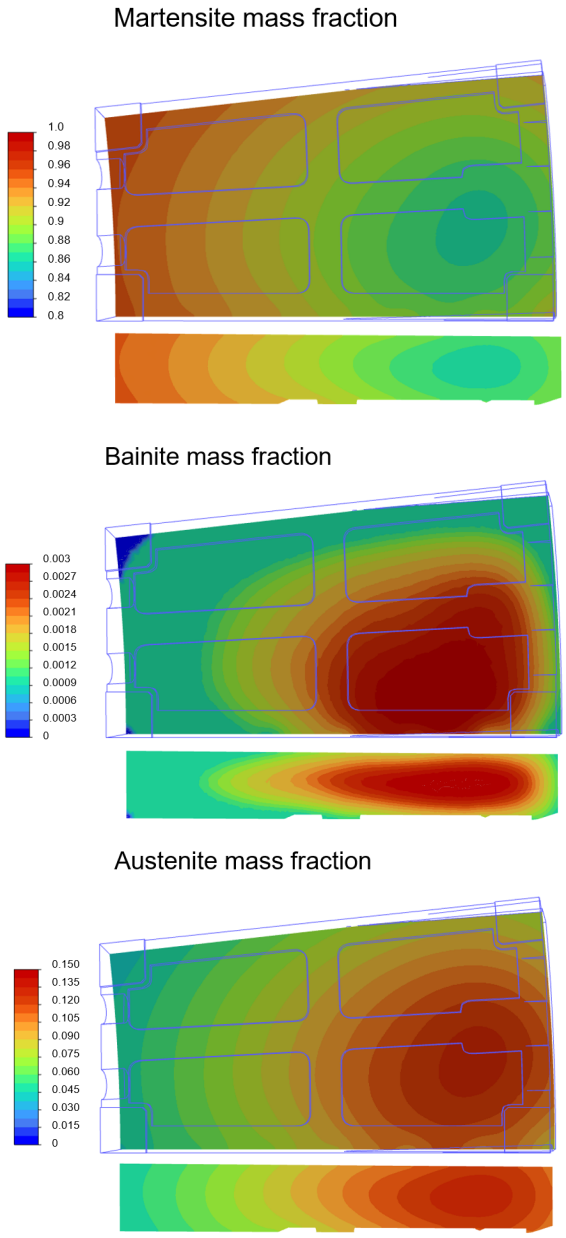

Figure 6.2. *Mass fractions of martensite, bainite and austenite in the middle of the component after 3.5 h cooling in the initial forced convection simulation.*

6.2 Improvements to forced convection simulation with solids-only model and full model simulation

In order to improve the accuracy of cooling, the correct emissivity for the radiation model is initially searched with a solids-only model to be of value 0.6 to reach the correct cooling rate with a cooling flow rate of 45 000 m^3/h. The cooling rate of the solids-only simulation with an emissivity of 0.6 compared to the emissivity of 0.95 used in the initial forced convection simulation is presented in figure 6.3. The reason for this low of an emissivity could be an oxide layer forming on the surface since usually used emissivity for this type

of steel is 0.95.

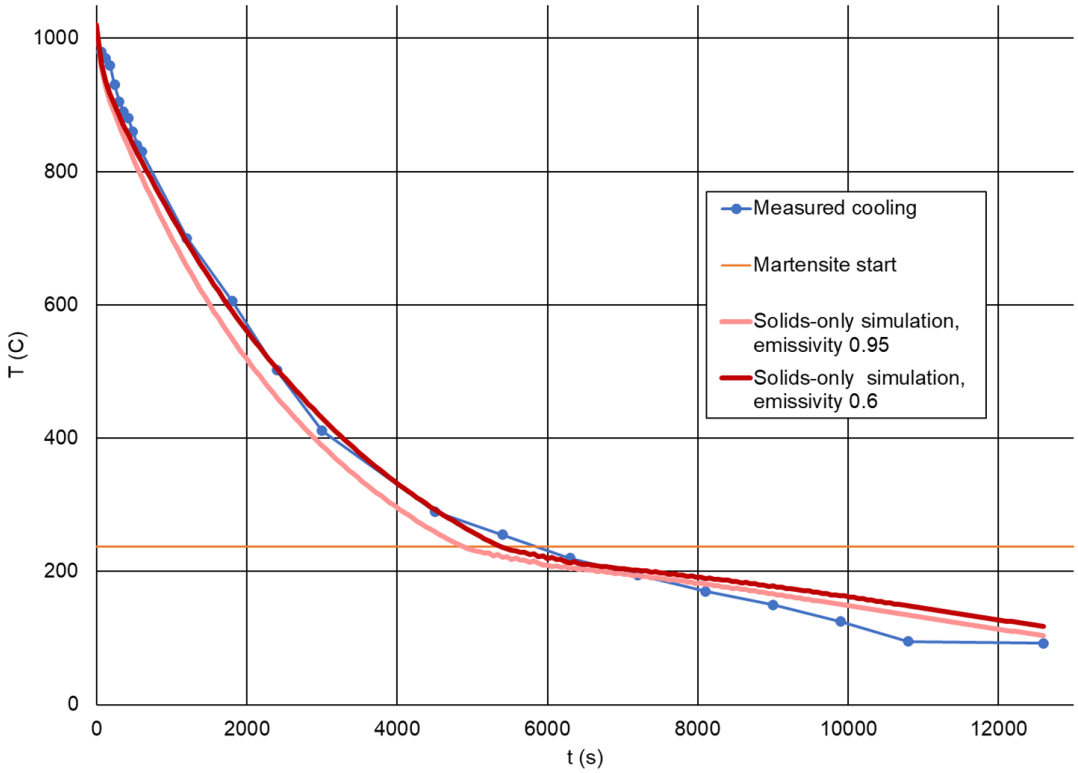

Figure 6.3. *Cooling rate of solids-only model forced convection simulation calculated with an emissivity of 0.6 and 0.95 with Scalable Wall Functions at a cooling flow rate of 45,000 m^3/h, time step size 60 s.*

The cooling rate simulated with the emissivity of 0.6 seems to follow the measurements well up until the measurement at 5,400 s, where the measured temperature is 255 °C but the simulated value is 236.7 °C. The reason for this difference seems to be that in the simulation the start temperature of martensitic transformation acquired from JMatPro is lower than would be expected based on the measured cooling. The temperature measured at 5,400 s is above the martensitic start temperature 236.8 °C, but the slowing effect to the cooling caused by martensitic transformation has already begun.

The largest differences between the simulation and the measurements are at 5,400 s and 10,800 s, the latter of which could be partly due to inaccuracy in the measured temperature since the measured value is lower than would be expected based on the surrounding measurements. The temperature of the component seems to be overestimated by the simulation after the start of martensitic transformation but approaches the correct cooling after most of the transformation has occurred.

The mass fractions of martensite, bainite and austenite after 3.5 h of cooling are similar to those of the initial forced convection simulation with different wall treatment and not accurate fan properties, as can be seen from figure 6.4. As was predicted in section 6.1, slightly more bainite is formed with an accurate cooling rate. The maximum mass

fraction value of bainite is 0.008, which is still small, although it is 3 times as large as the maximum value for bainite mass fraction in the initial simulation.

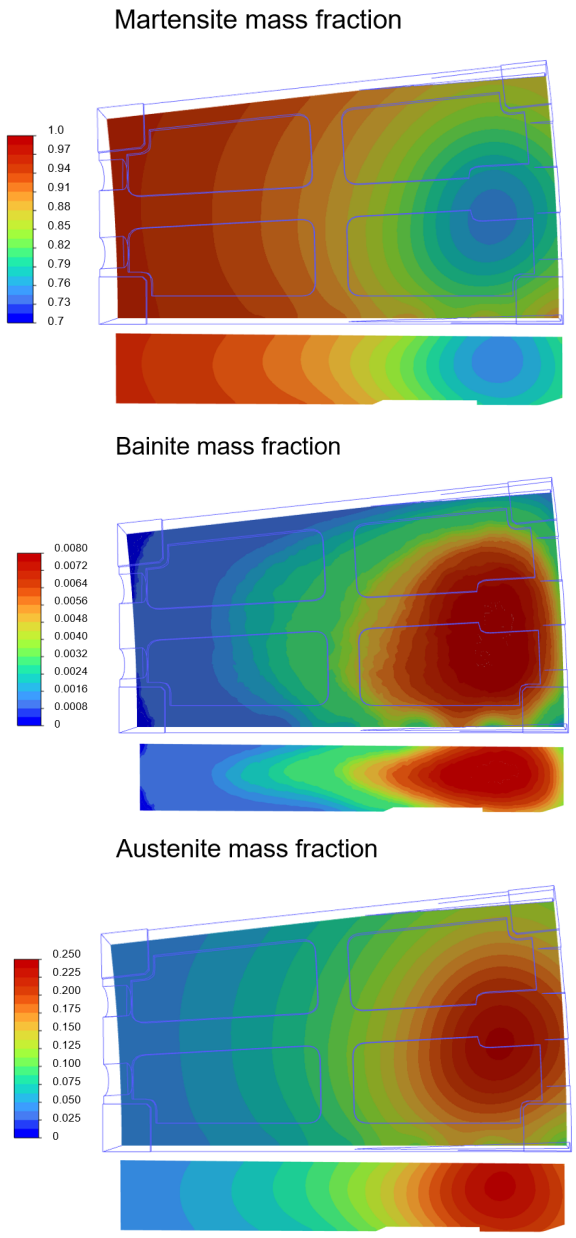

Figure 6.4. *Mass fractions of martensite, bainite and austenite in the middle of the component after 3.5 h cooling in solids-only forced convection simulation with emissivity of 0.6.*

Another thing that can be noticed when comparing the mass fractions of solids-only simulation from figure 6.4 to those of the initial simulation from figure 6.2, is that there is more austenite left in the initial forced convection simulation after 3.5 h than in solids-only simulation. The mass fraction of austenite left is 0.115. The larger amount of austenite is explained by slower cooling since despite the end temperatures of the measure points being quite similar (99 °C for the initial simulation and 117 °C for the solids-only simulation), the maximum temperature in the components is 151.75 °C when in the initial simulation it

was only 117.15 °C. The maximum temperature is below the start temperature of martensitic transformation, so if the component is left to cool to room temperature, the austenite will transform only to martensite, so the fraction of martensite may increase, but not the fraction of bainite.

After the initial search of the correct emissivity with the solids-only model, the simulation is carried out once again the same way as in the initial simulation, establishing the flow field in steady-state simulation and then carrying out the transient simulation with a frozen flow field to acquire sensible simulation time. As can be assumed, the simulation initially follows the solids-only model quite well, since the heat transfer coefficient and radiation values for the solids-only model are taken from the initial state. As time goes on and the component cools down, the full simulation result starts to slightly drift away from the solids-only simulation result. The cooling is slightly quicker in full simulation. The full simulation cooling curve compared to the measured cooling is depicted in figure 6.5.

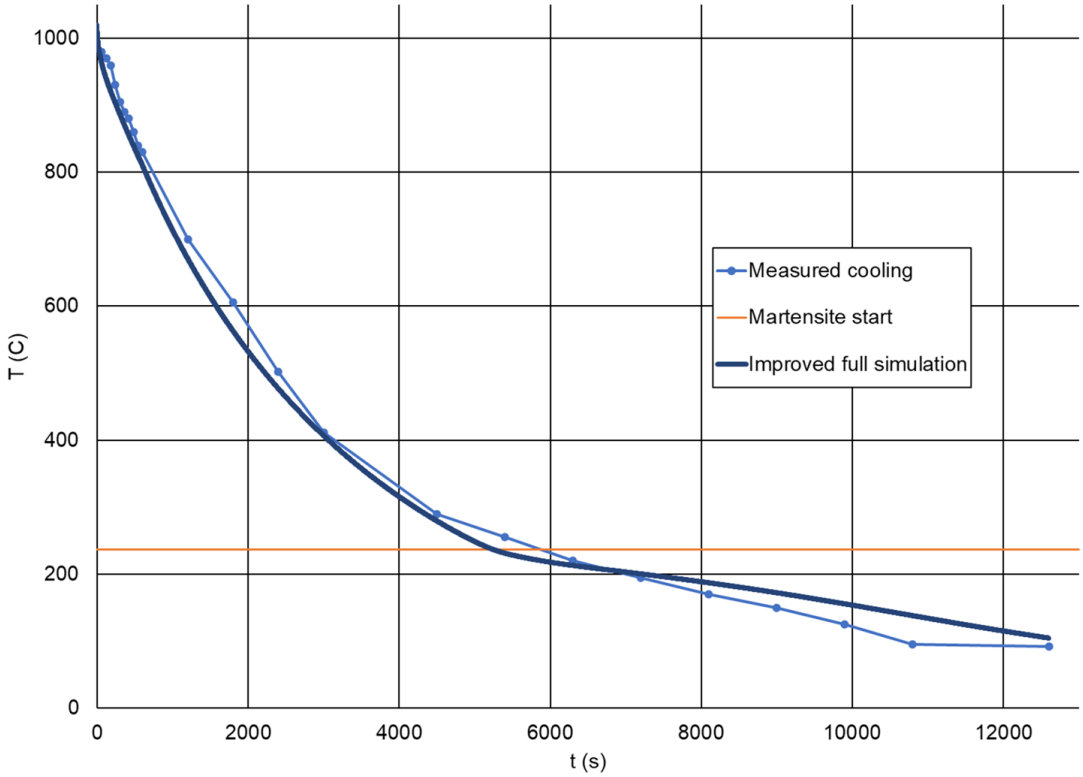

Figure 6.5. *Cooling rate of the forced convection simulation calculated with fluid included and with an emissivity of 0.6 and Scalable Wall Functions at a cooling flow rate of 45,000 m^3/h, time step size 0.1 s for first 20 steps and after those 1 s.*

The conclusions about the effect of too low martensitic start temperature that were made for the solids-only model hold also for the full model. If the martensitic transformation were modified to start earlier than the temperature JMatPro provides based on the material composition, it can be hypothesized that this would improve the accuracy of the simulation, since the martensitic transformation would slow the cooling at higher temper-

atures. As can be seen from figure 6.5, the slowing effect is now occurring too late and at lower temperatures than desired, which leads the cooling at the end of the simulation to be too slow in comparison to the measured data.

The mass fractions at the end of the full simulation can be seen in figure 6.6. The mass fraction of formed bainite is 0.0024, and as can be noticed when comparing to the solids-only model results in figure 6.4, the amount of formed bainite is at maximum 0.006, less than in solids-only simulation, which is the result of slightly quicker cooling. The maximum mass fraction of austenite at the end of the full simulation is 0.138, which is once again less than in solids-only simulation, and is due to the maximum temperature at the end of the simulation being 119 °C, about 30 °C lower than in solids-only simulation.

If the temperature data and mass fractions from the simulation are analyzed together and compared to the cooling measurements, it is noticed that the slowing of the cooling is not occurring at the same temperature in the simulation as in the measured data. As was discussed, this is assumed to be due to the start temperature of martensitic transformation being higher than JMatPro suggests. The rise in the martensitic start temperature could also be accounted for the segregation, which could mean that also the formation of bainite differs from the nominal composition.

In figure 6.7 the initial, 0.95 emissivity and final, 0.60 emissivity solids-only model simulations are compared to the full simulation with 0.6 emissivity and to the measured data. Both the solids-only simulation and full simulation with an emissivity of 0.6 correlate better with measured data cooling before phase transformations than the initial guess of 0.95 emissivity solids-only model, but the full model cools at a slightly higher rate.

As can be seen from figure 6.7, at the beginning of the simulation, both the solids-only model and the full model cool at a similar rate, but around 800 °C they start to deviate. In the solids-only simulation, the heat transfer is calculated correctly only at the initial temperature and since the frozen flow field is not exactly the same as a boundary condition of constant heat transfer coefficient on the solid surface. This is the reason why it drifts away from the full model at lower temperatures. After the start of martensitic transformation, the solids-only model with 0.95 emissivity gives slightly closer values when compared to the measured cooling, but the differences are small. It should be noticed, that since the full simulation with 0.6 emissivity cools faster than the solids-only simulation with 0.6 emissivity, also the full simulation with 0.95 emissivity would cool faster than its solids-only counterpart. The full simulation with 0.6 emissivity and solids-only simulation with 0.95 emissivity reach the same end temperature of 104 °C.

The results in figure 6.7 are affected by the parameters of the fan model which are somewhat uncertain. The location of the fan and the shape of the blade are only estimations, and the flow field caused by the fan seems to change slightly with time because the geometry causes swirls to the flow field. The swirls can differ from the measured case if,

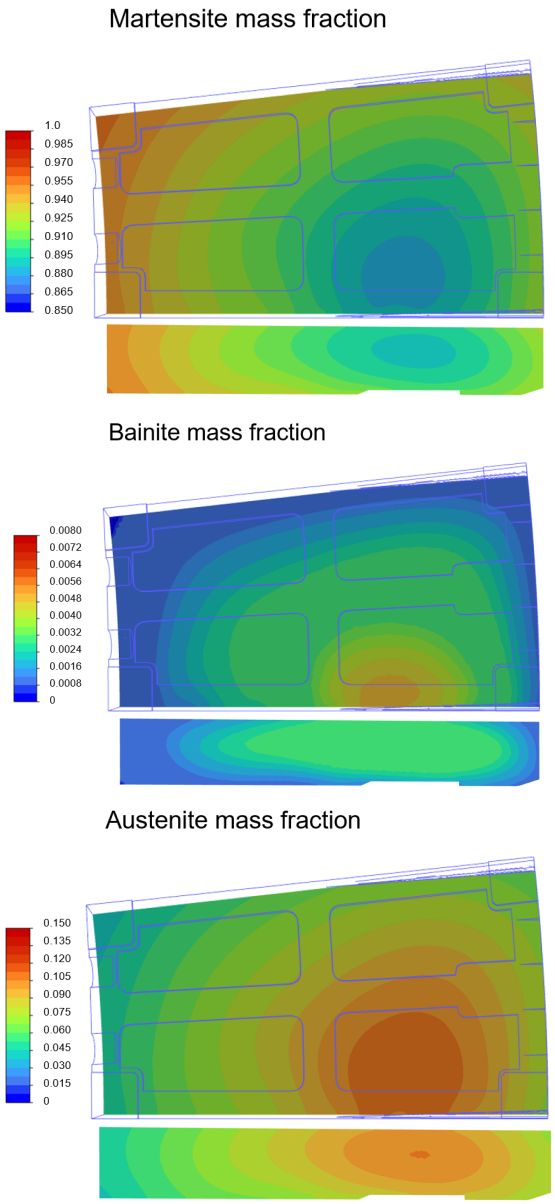

Figure 6.6. *Mass fractions of martensite, bainite and austenite in the middle of the component after 3.5 h cooling in forced convection simulation with the full model and emissivity of 0.6.*

for example, the angle and position components or the fan is just slightly different from what is modeled in this case. This means that freezing the flow field will be only averagely correct and these uncertainties cause inevitable deviation to the measured data.

In a study by Shang and Z. J. Wang (2010), the cooling of their component is very quick and the formation of bainite is avoided, as was mentioned in section 4.4. Average error between the simulation and the measured data in their study was 7.9 %. In the current thesis simulation of the forced convection case, average error is 7.4 %, so the error is in same order of magnitude as in the study by Shang and Z. J. Wang (2010). The root mean squared error is 24.2 °C.

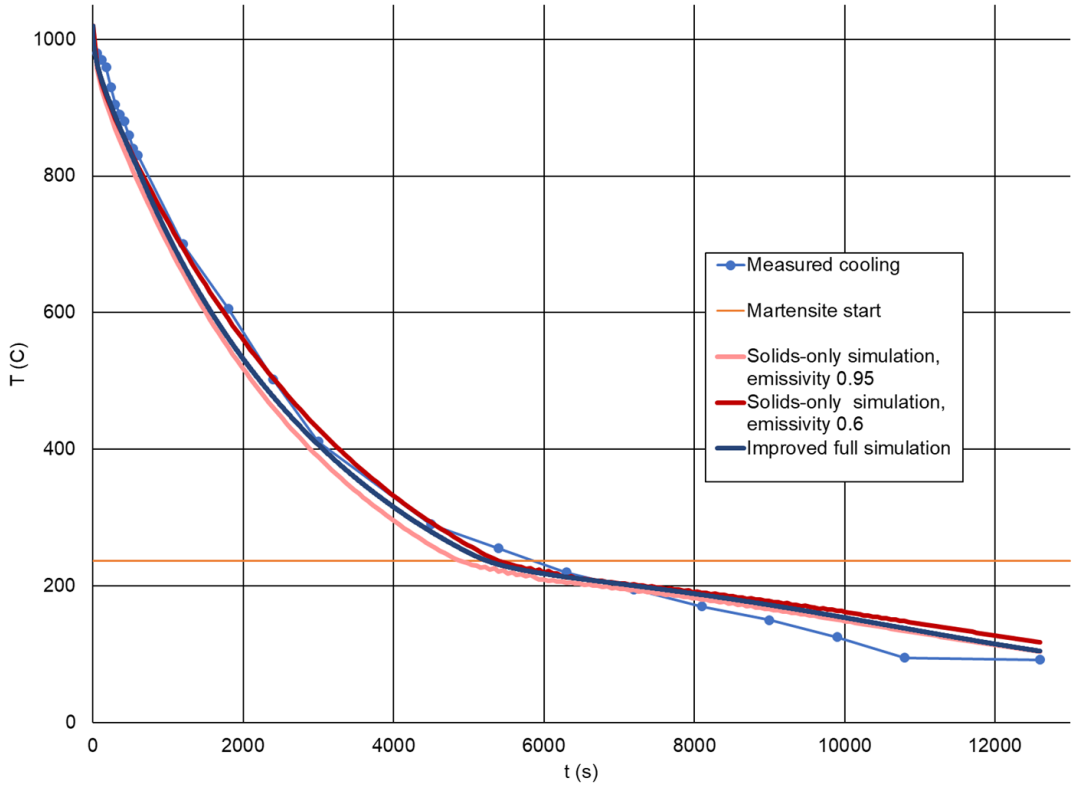

Figure 6.7. *Comparison of the initial forced cooling solids-only simulation with an emissivity of 0.95 to improved solids-only and full simulation, both with an emissivity of 0.6.*

6.3 Initial natural convection simulation

The cooling rate of the natural convection simulation in comparison to the measurement data is shown in figure 6.8. The start temperatures of the bainitic and martensitic transformation also depicted in figure 6.8 underline the need for taking segregation into account. It is clearly seen that the latent heat release from martensitic transformation occurs at too low temperatures. This is also the case for the bainitic transformation, and as can be noticed from the figure, the start of the bainitic transformation needs to also be shifted to start earlier, since with the simulated amount of bainitic transformation clearly not enough latent heat is released.

Outside the slowing effect of the latent heat of martensitic and bainitic transformation occurring at too low temperatures, the cooling curve correlates well with the measured data. Since the uncertainty of the fan is not included in this simulation, it is easier to detect the issues of not including segregation in the simulation. It can also be noticed that the deviating effect of segregation only affects a small portion of the calculation. Therefore it can be estimated that since the phase transformations only occur at a specific temperature range, the cooling of the component surface follows the cooling of the rest of the volume as well after most of the transformations have occurred, even though the transformations start at the wrong temperatures.

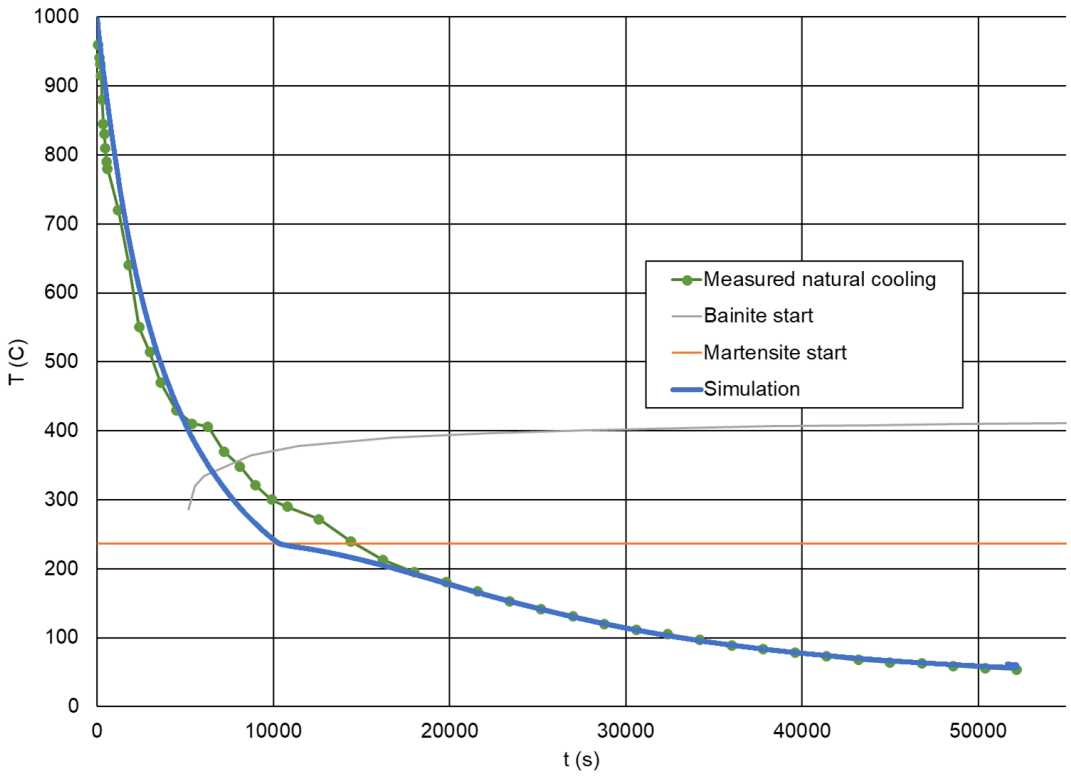

Figure 6.8. *Cooling rate of the measured point in initial natural convection simulation and the measured data, initial time step size 1 s, which is then increased to 10 s.*

Since the simulated result does not follow the measurements well in the transformation area, it is likely that at least the mass fraction of bainite is incorrect, as not enough bainite is formed to cause a slowing effect on the cooling curve. However, the scale of the latent heat released is correctly calculated, because despite less bainite forming than expected, released heat from the martensitic formation slows the cooling the right amount to catch the measured cooling curve. Before the beginning of bainitic transformation and after the biggest effect of the martensitic transformation, the cooling curve follows the measurements well. The mass fractions are presented in figure 6.9.

The mass fraction of bainite in the components after 14.5 h of cooling is 0.013, quite evenly distributed since the maximum in any cell in the component is 0.014, so compared to the amount of bainite formed in the forced convection case the amount has almost doubled. Since the cooling time is 4 times longer than that of the forced convection case, also a lot more austenite has transformed. The mass fraction of austenite that is left after 14.5 h is 0.047 and maximum 0.049, so cooling to a lower temperature reduces the amount of austenite to one-third in comparison to the forced cooling case despite the cooling being a lot slower. Still, it needs to be taken into account that also the component geometry is different in these simulations, so it can not be directly compared. After 3.5 h of natural cooling, the amount of austenite left is 0.73. The martensite mass fraction formed after 14.5 h is 0.94 and the maximum is 0.95, so the amount of formed martensite

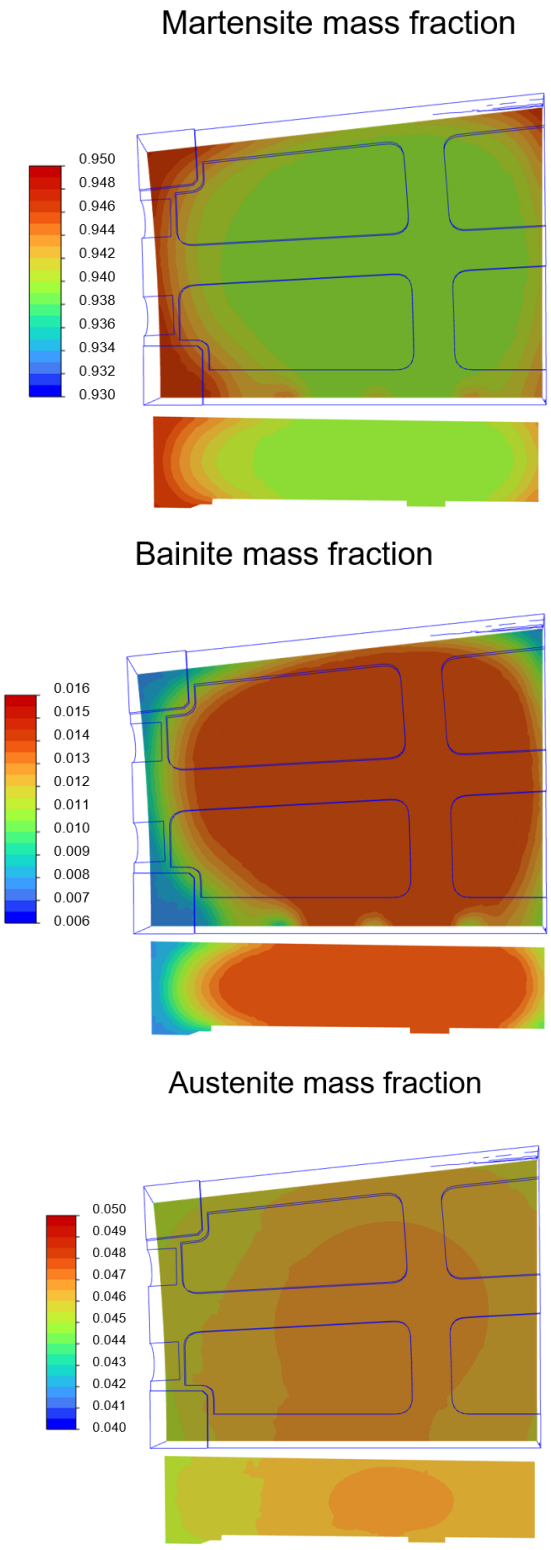

Figure 6.9. *Mass fractions of martensite, bainite and austenite in the middle of the component after 14.5 h cooling in initial natural convection simulation.*

is slightly lower than in the forced convection case.

The results of this simulation raise the need to examine the effect of segregation and more

specifically what is the impact it has on the overall simulation. The hypothesized result of the simulation that includes segregation is that the amount of bainite increases vastly in the component. If this is the case, in a possible simulation case where the question would be, for example, how long does it take to cool a component and not how much bainite and martensite are formed, the effect of segregation does not need to be simulated.

6.4 Inclusion of segregation by separated volume to natural convection simulation

The resulting cooling curves for the simulations, where material properties of the segregated composition are implemented to the surface volume 10 mm and 20 mm from the surface of the components, are depicted in figure 6.10. As can be seen, the inclusion of fabricated segregation results in the slowing effect caused by the bainitic formation in segregated areas appearing in the cooling curve. The scale of the slowing effect of the segregated bainitic transformation in volume 20 mm from the surface is correct, but the slowing effect of martensitic transformation appears at too low a temperature. The reason for this is suspected to be that the martensitic start temperature acquired from JMatPro is too low. As can be seen from figure 6.10, the simulation where the segregated volume is only 10 mm from the surface does not produce enough bainite to match the measured cooling rate.

The mass fractions of formed bainite after 14.5 h of cooling in initial, unsegregated simulation and segregated simulations 10 mm and 20 mm from the surface can be seen in figure 6.11. As can be seen, in the segregated areas a lot more bainite is formed in comparison to unsegregated areas. The reason why more bainite is forming near the bottom of the component in segregated simulations is that the furnace tray keeps the bottom of the component hot for longer, and the heat from the bainitic transformation is released upwards through the component.

The average mass fraction of formed bainite in the initial, unsegregated simulation is 0.013, in the simulation with 10 mm from surface segregated volume 0.12 and in the simulation with 20 mm surface segregated volume 0.28. Since the simulation with 20 mm surface segregated volume reaches the measured cooling curve, as can be seen from figure 6.10, it can be concluded that the amount of bainite in this simulation is correct. However, the distribution of the bainite in the component needs to be examined more closely.

From all of the segregated simulations in figure 6.11, it can be seen quite clearly where the segregated surface volume starts. This sharp of change is not realistic, and it is likely that the effects of segregation are exaggerated in the surface volume near the rest of the volume and vice versa, on the outer border of the inner volume, it is likely that the

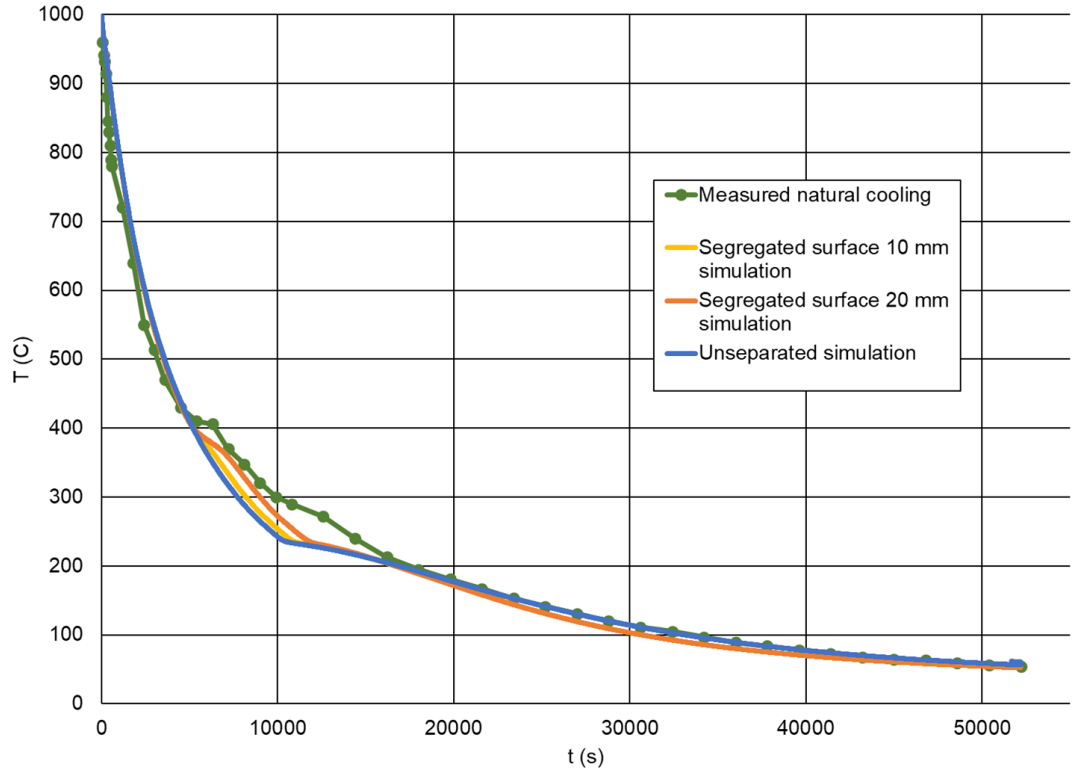

Figure 6.10. *Cooling rate of the measured point in natural convection simulation, when segregated material properties are assigned to volumes up to 10 mm and 20 mm from surface and the measured data, initial time step size 5 s, which is then increased to 10 s.*

effect of segregation is undermined. In reality segregation is more pronounced deeper in the section, whereas near the surface segregation effects does not significantly occur or at least annealing treatments carried out before cooling can even up the small local differences in elemental gradients.

Since the distribution of segregated areas is not accurately depicted by separating a volume from the component and assigning segregated material to that volume, another way of simulating the effect of segregation and different grain sizes needs to be examined. A way of simulating the effect by only using the original material properties should be preferred since the composition and grain size of the segregated material are not known exactly and need to be searched for. This is time-consuming and results of a quicker way of simulating the effect are presented in section 6.5.

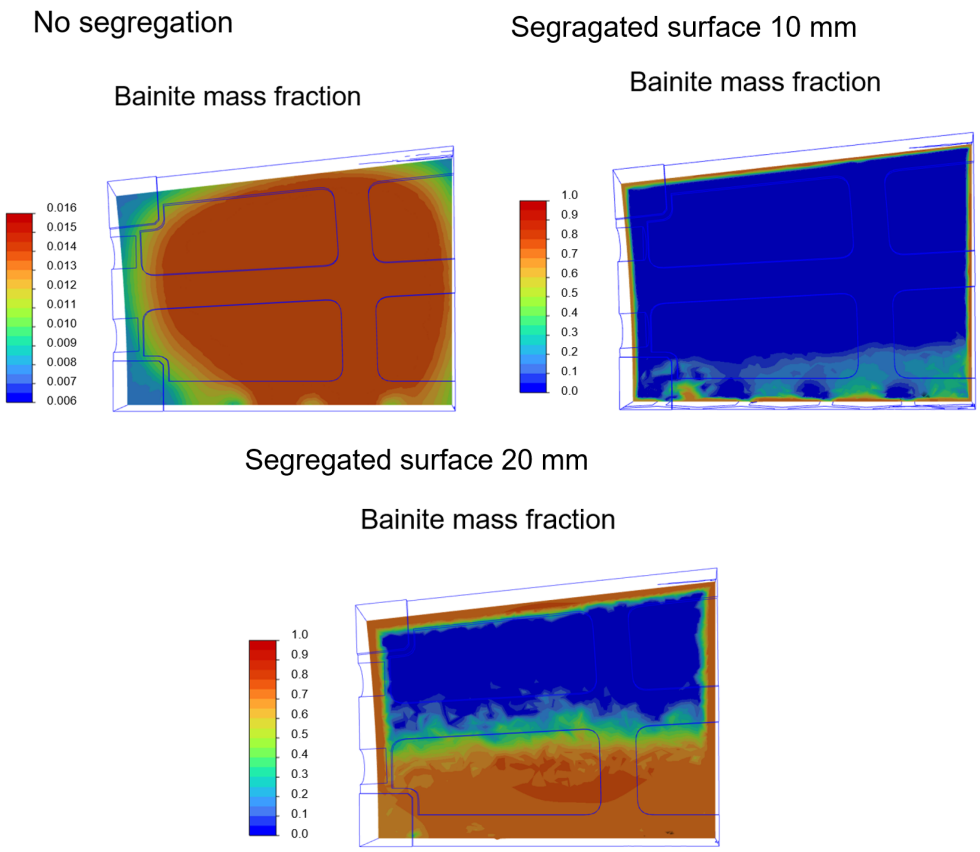

Figure 6.11. *Mass fractions of bainite in the middle of the component after 14.5 h cooling in natural convection simulation, with no segregation, segregation assigned to volume 10 mm from surface and 20 mm from surface.*

6.5 Inclusion of segregation by modified starting time to natural convection simulation

As was discussed in section 5.5, the main issue with the original material composition and grain size is that based on it not enough bainite is formed. This issue is tackled by modifying the starting time of the simulation. The resulting cooling curve is depicted in figure 6.12, where the starting time of cooling is set to 0 s. The simulation starting time was set to 18,000 s instead of 0 s, but this is only a way of shifting the bainitic transformation curve to start earlier without modifying the material properties of the original material.

The resulting cooling curve seems to follow the measured cooling quite well, although the bainitic and martensitic transformations seem still to have too low starting temperatures. The low start of martensitic transformation seems to be due to JMatPro underestimation, but this and the higher bainitic start temperature are also due to the material being segregated and the carbide formation. The amount of bainite seems to be slightly too low since the simulation cooling curve does not reach the measured cooling curve during the

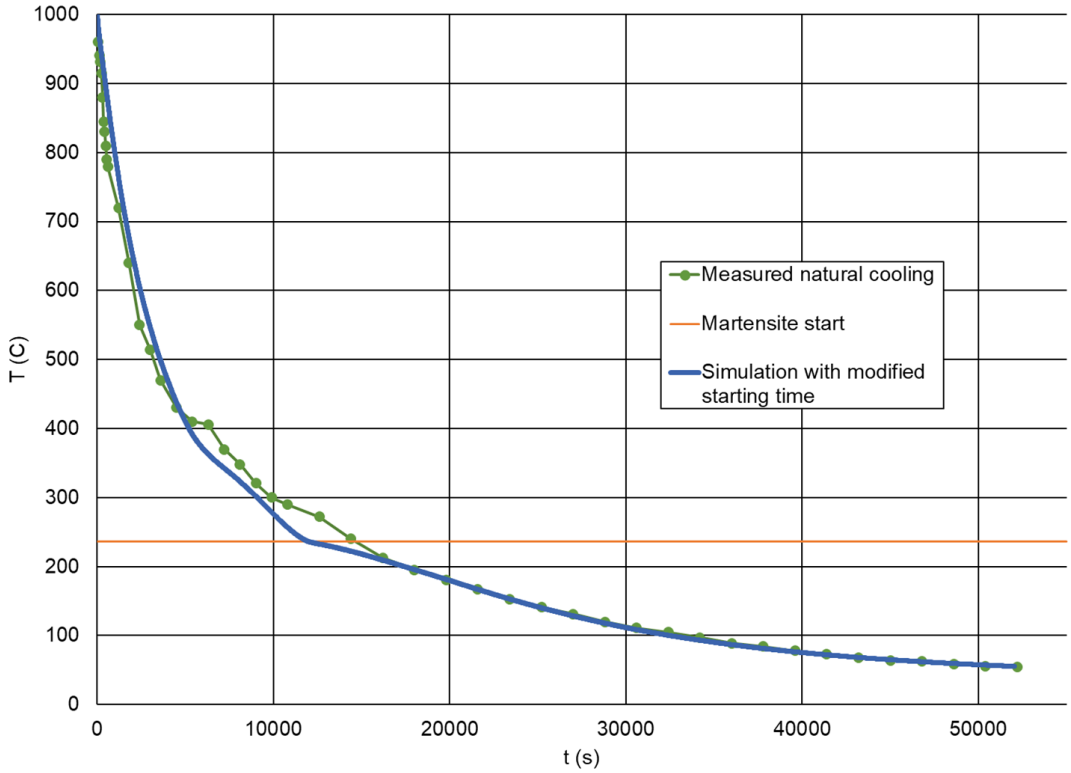

Figure 6.12. *Cooling rate of the measured point in initial natural convection simulation with the modified simulation start time set to 18,000 s and the measured data. The starting time is set to 0 s in this figure for clarity. Initial time step size is 5 s, which is then increased to 20 s.*

release of latent heat from bainitic transformation between 240–440 °C. This is due to the amount of formed bainite being slightly too small to release enough latent heat, the mass fraction being 0.23 of the initial austenite, as can also be seen from figure 6.13.

The distribution of phases is more accurate than in simulations with separated volumes of segregated material properties in section 6.4. Based on the results, the approach to the segregation and modifying grain sizes by modifying the starting time is working as expected. Since the start temperature of martensitic transformation is still remarkably lower, a simulation is conducted where the start temperature of martensitic transformation is calculated with equation 2.9. The simulation starting time must also be slightly modified, to ensure the formation of a sufficient amount of bainite.

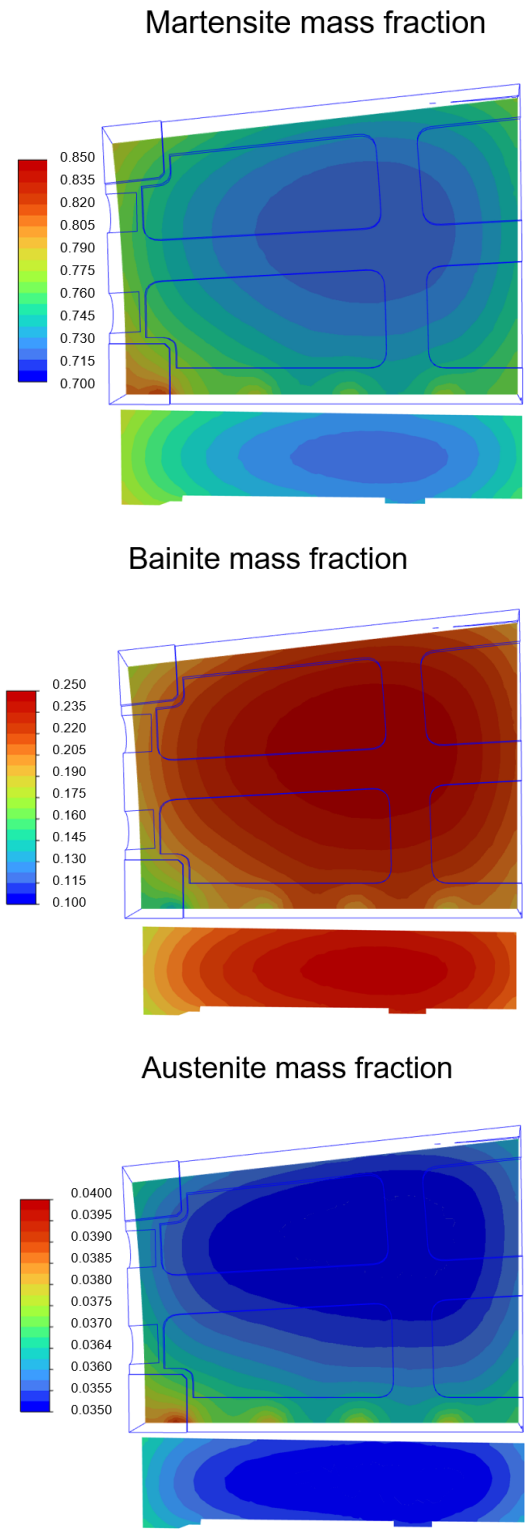

Figure 6.13. *Mass fractions of bainite, martensite and austenite in the middle of the component after 14.5 h cooling in natural convection simulation, with modified starting time.*

6.6 Final forced and natural convection simulations with increased martensitic transformation start temperature

As can be seen from figure 6.14, lifting the starting temperature of martensitic transformation to 293.9 °C improves the accuracy of the natural convection simulation. In this simulation, also the starting time of the simulation was moved forward to 20,000 s, for enough bainite to form. This seems to form an accurate amount of bainite but since the rise in bainitic transformation starting temperature due to segregation and carbide formation is not taken into account, bainite forms in the simulation at a lower temperature than the measured data suggests.

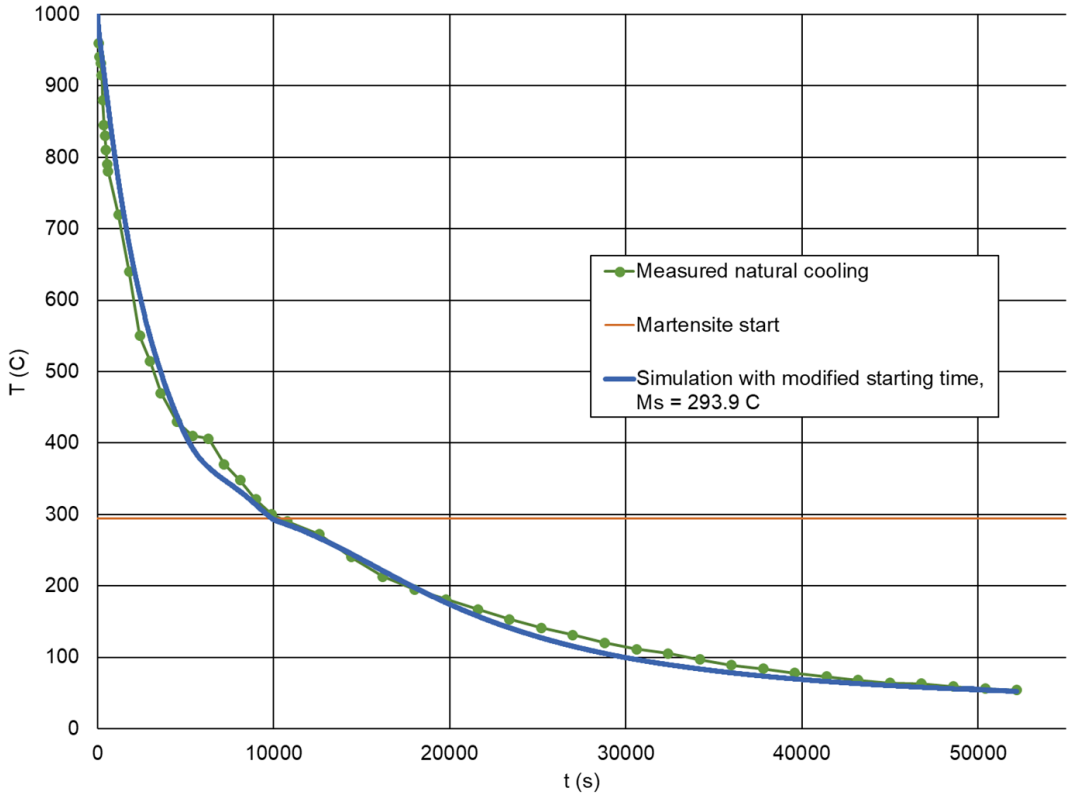

Figure 6.14. *Cooling rate of the measured point in initial natural convection simulation with the modified simulation start time set to 20,000 s, martensitic start temperature set to 293.9 °C and the measured data. The starting time is set to 0 s in this figure for clarity. Initial time step size 5 s, which is then increased to 20 s.*

The average mass fraction of formed bainite is now 0.25, and the distribution of bainite and other phases can be seen from figure 6.15. When compared to the simulation with a modified starting time but lower martensitic start temperature, the differences in phases after 14.5 h of natural cooling are small. Slightly more bainite is formed, slightly less martensite and slightly less austenite is left.

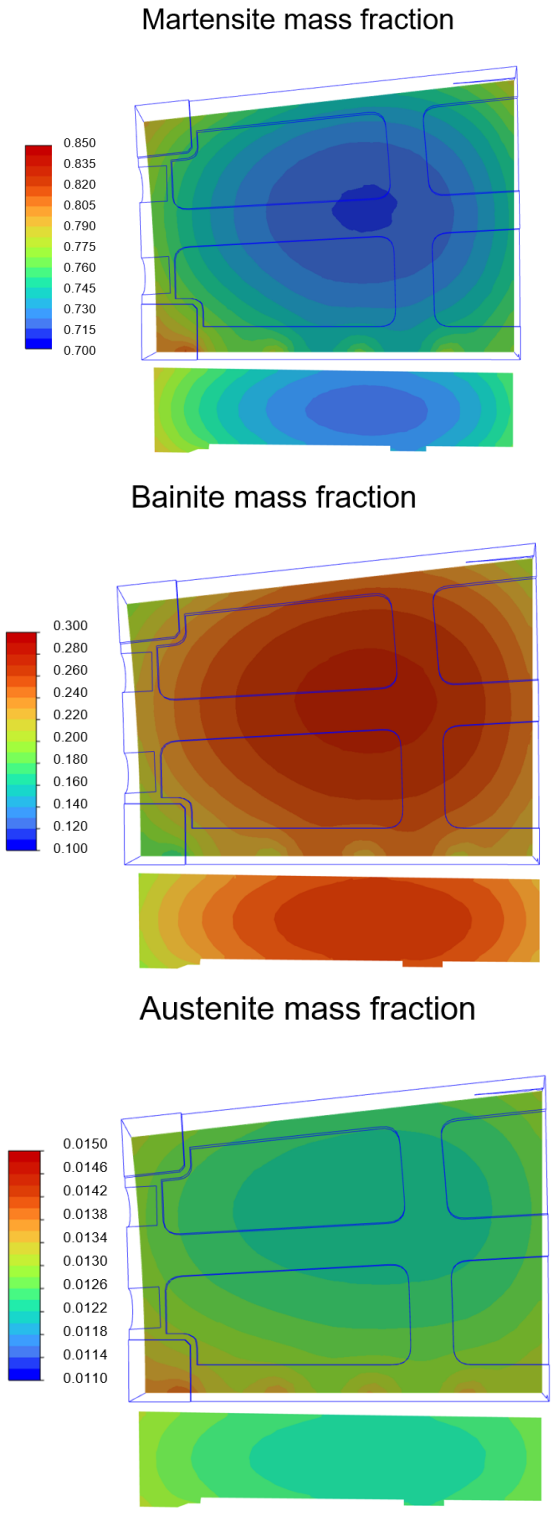

Figure 6.15. *Mass fractions of bainite, martensite and austenite in the middle of the component after 14.5 h cooling in natural convection simulation, with modified starting time and martensitic transformation start temperature of 293.9 °C.*

It can be concluded that using a correlation for the martensitic transformation starting temperature improves the accuracy when comparing the cooling curves to the measured

data. Still, this seems to have little effect on the final phase distribution. As in the simulation with only a modified starting time in section 6.5, it can be seen that modifying the starting time of the simulation gives a realistic distribution of phases. Thus, it is a possibility for modifying the simulation if the original material properties do not seem to provide accurate results due to the heterogeneity of the material.

The result of increasing the martensitic transformation starting temperature in forced convection simulation can be seen in figure 6.16, where also the simulation with a lower martensitic transformation starting temperature is illustrated. It can be noticed that despite the point where the cooling rate starts to slow down is more accurate with a higher martensitic start temperature, the is not a drastic change in accuracy. Both simulations seem to overestimate the slowing effect that martensitic transformation has on the cooling rate. This can be due to the used martensitic transformation coefficient α correlation overestimation. The average error in natural convection cooling simulation in comparison to the measured data is 7.1 % and the root mean squared error is 35.8 °C.

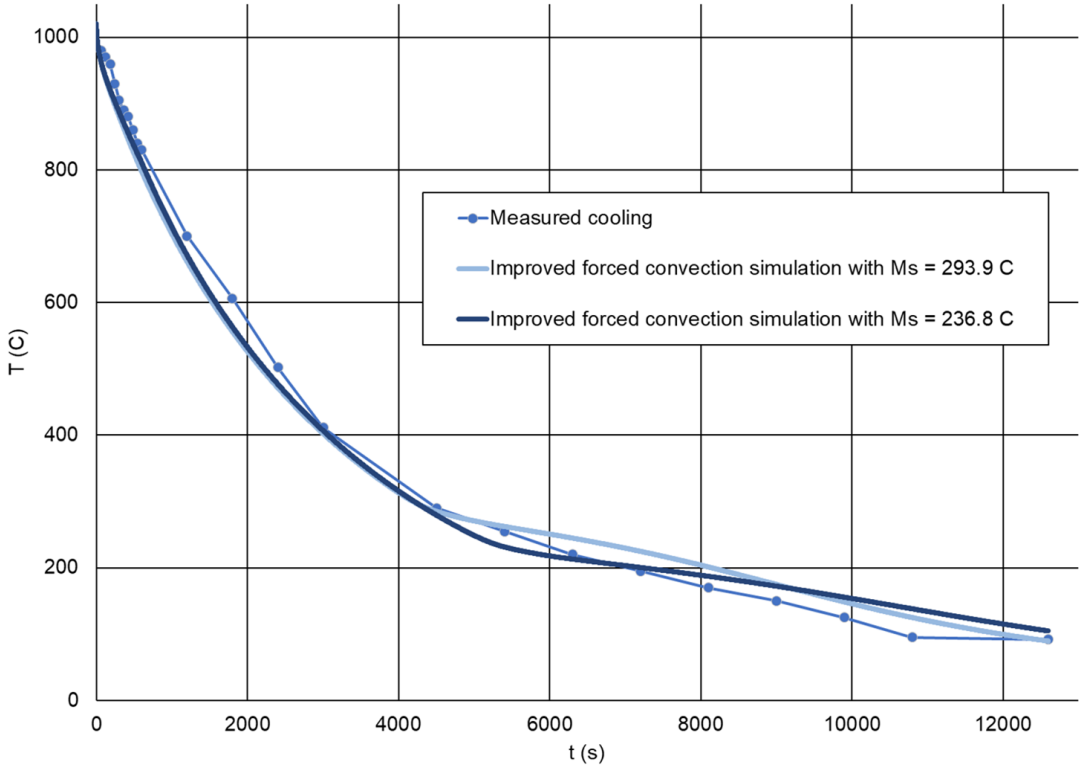

Figure 6.16. *Cooling rates of the measured point calculated with an emissivity of 0.6 at a cooling flow rate of 45,000 m^3/h with the martensitic start temperatures 236.8 °C and 293.9 °C. Initial time step size 0.1 s, which is then increased to 1 s.*

As was the case with natural convection, the mass fractions or distribution of phases do not change drastically when the start temperature of martensitic transformation is increased. The mass fraction of formed bainite is 0.0016, so the absolute change is small to 0.0024 fraction of the simulation with the original martensitic transformation start. The

distribution of phases is depicted in figure 6.17.

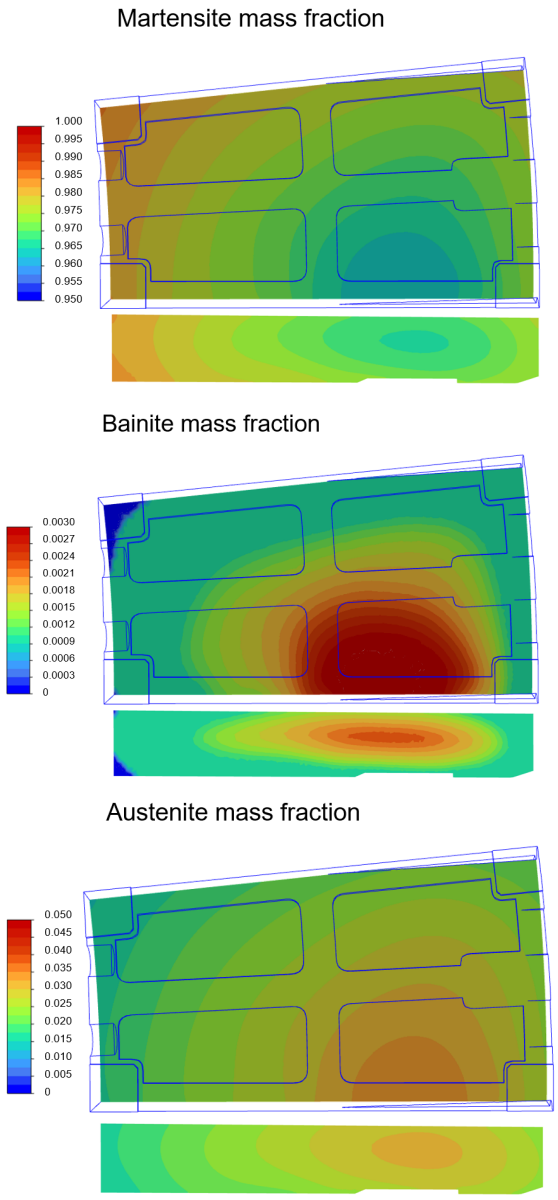

Figure 6.17. *Mass fractions of bainite, martensite and austenite in the middle of the component after 3.5 h cooling in forced convection simulation, with martensitic transformation start temperature of 293.9 °C.*

Overall, as was also noticed with natural convection, lifting the martensitic start temperature does not change the phase distribution or mass fractions at the end of the simulation remarkably. In natural convection, the most significant effect was on the accuracy of the cooling rate in comparison to the measured data. The forced convection cooling rate does not improve, although the start of the slowing due to martensitic transformation is more accurate, as can be seen from figure 6.16. Average error between measured data and simulation in cooling in the forced convection simulation with higher martensitic start temperature is 7.9 % marginally larger than in the simulation 6.3. The root mean squared error of this simulation is 29.2 °C.

The inaccuracy caused by the frozen flow field is investigated. As can be seen from figure 6.18, the cooling rates of frozen and non-frozen flow fields start to drift apart after a while. This reinforces the notion that the fan brings uncertainty to the simulation since the rate of cooling varies a lot. The non-frozen simulation seems to be slightly more accurate after the start of martensitic transformations, though it is more erroneous at the beginning of cooling. On average, the frozen flow seems to be more accurate, so most likely in reality the flow is slightly disturbed or the fan is not quite as effective, which causes slower cooling in the measured data after the start of the cooling. Overall, the non-frozen flow should be more accurate, since it can take into account the changes in the flow field, but also it is more easily disturbed by bigger time step sizes or deviations in geometry, and the non-frozen simulation is also more time-consuming.

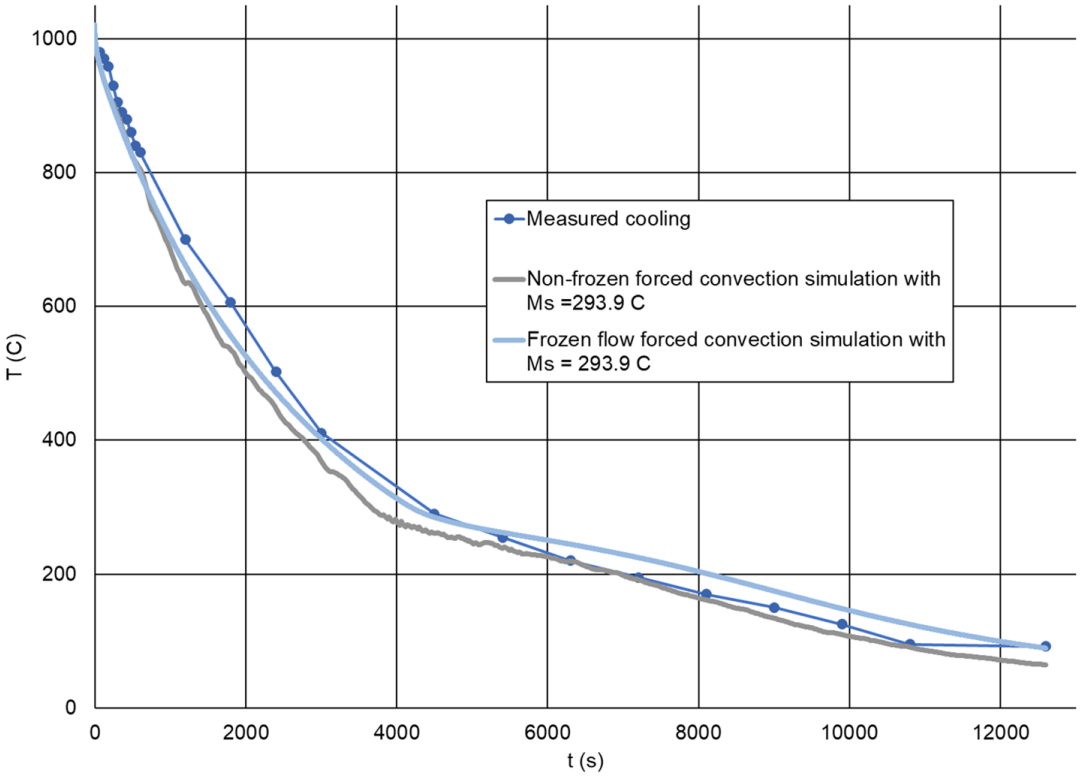

Figure 6.18. *Comparison of the non-frozen and frozen flow forced convection simulation cooling rates with martensitic start temperature set to 293.9 °C. Initial time step size for non-frozen flow initially 1 s, which is then increased to 10 s.*

The average error between measured data and simulation is only 6.7 %, due to the end of the simulation correlating with the measured data extremely well. The root mean squared error is 32.5 °C. The mass fractions of the non-frozen flow forced convection simulation are depicted in figure 6.19. The mass fraction of bainite is 0.0012, so the change to the frozen flow simulation is small. Since the non-frozen flow simulation cooling is further away from the measured cooling than the frozen flow simulation cooling near the start of martensitic transformation, it can be assumed that these mass fractions are less accurate than the mass fraction in figure 6.17.

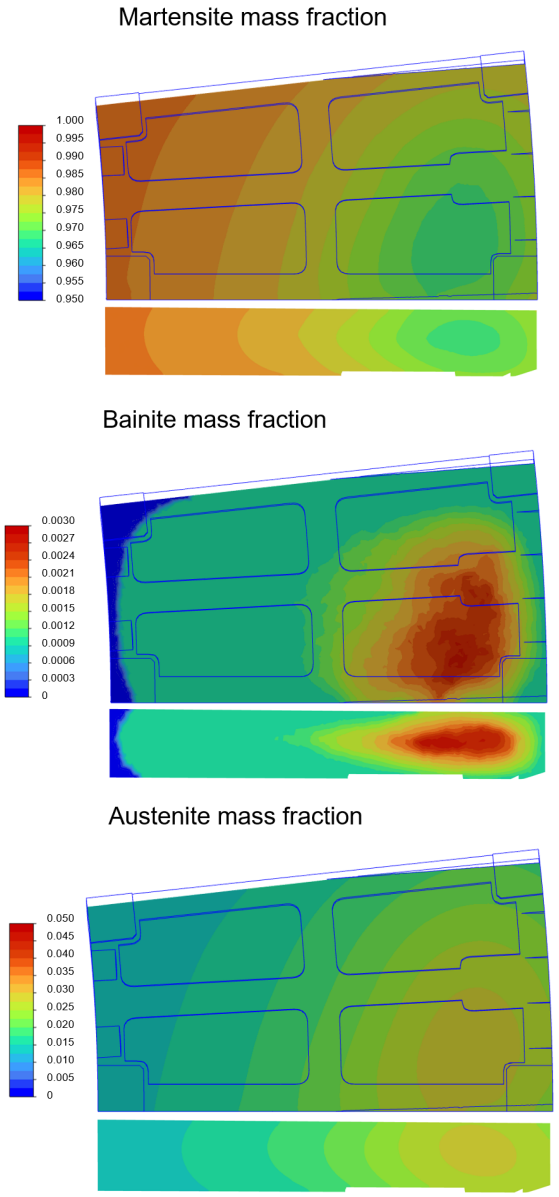

Figure 6.19. *Mass fractions of bainite, martensite and austenite in the middle of the component after 3.5 h cooling in non-frozen flow forced convection simulation, with martensitic transformation start temperature of 293.9 °C.*

The reasons why there is more inaccuracy in the results of forced convection simulation than those of natural convection are the inaccuracies related to fan modeling since the simulations fail to cool the component as quickly as measured when the martensitic transformation is occurring. The geometry and location of the fan and the shape of the blade are simplified and estimated, and the choice of modeling the fan as a 3D fan zone is also a simplification. Also, the differences in geometry of the simulation model to the measured setup create more inaccuracy than in the case of natural convection. The pressure jump across the 3D fan zone is expected to remain constant throughout the simulation, and the inflection point is set to the default 0.83 of the blade length since the exact shape of the blade is not known.

6.7 Key improvements of air quenching process modeling

The key factors for modeling the air quenching process with this steel type are depicted in figure 6.20. It is found in this thesis that an effective way of calculating the formed bainite is by interpolating the bainite mass fraction from constant cooling curves. The constant cooling curves collected from JMatPro should cover the area of the assumed slowest and quickest cooling rate in the time-temperature coordinate system, to ensure that the interpolation does not produce incorrect answers.

The use of the modified Koistinen and Marburger equation 2.10 is also found to be an effective way of modeling martensitic transformation, which is easier to describe using an equation since the amount of formed martensite is not time-dependent. The used correlation for the martensitic transformation constant α might be slightly too steep, which can cause the slowing effect of martensitic formation in forced convection to be slightly too large. A correlation for calculating the martensitic start temperature should be used, for example the one used in the thesis in equation 2.9. The calculation of the amounts of bainite and martensite should take into account the formed fraction of the other phase to ensure mass balance within the calculated cell. The magnitude of the latent heat released from phase transformations with the calculation methods used seems to be correct, so the method of halving the released heat used in the study by Takeuchi and Yogo (2021) is not needed.

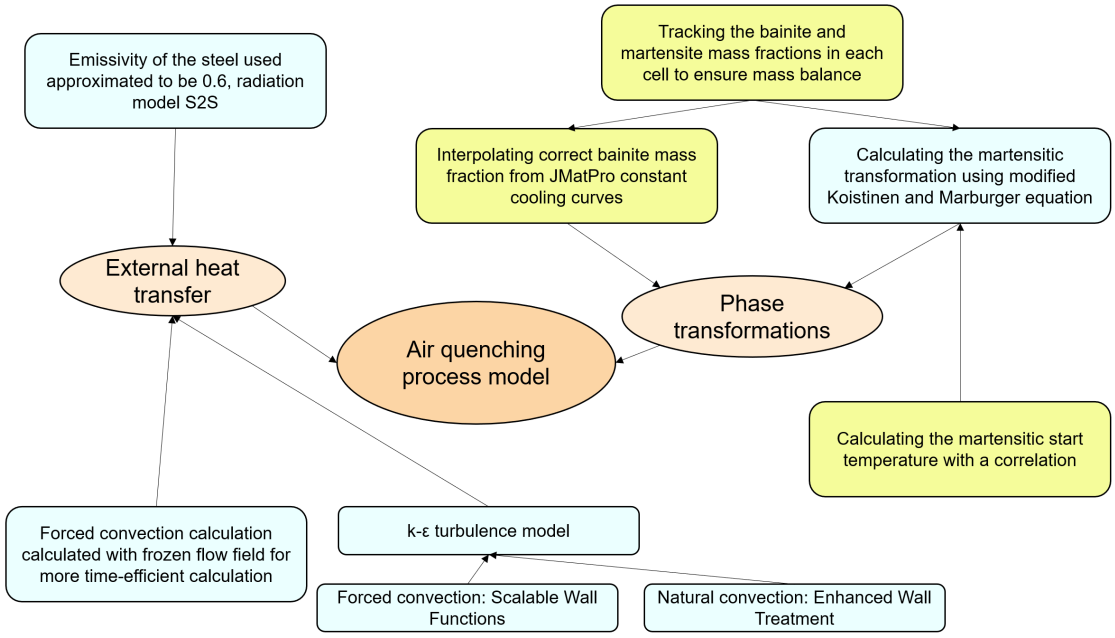

Figure 6.20. *Factors for improved steel casting parts air quenching process simulation found in this thesis. The main improvements made are colored yellow.*

The factors of external heat transfer that are brought up in this thesis are that for the radiation model S2S, the emissivity that should be assigned for this type of steel is ap-

proximated to be 0.6. This can be used as a starting point for other simulations of similar steel types and the more exact emissivity can be searched with a solids-only simulation. It must be noticed that the emissivity of the steel can vary depending on the steel used and the oxide layer forming on top of it, so the suitability of this emissivity should be evaluated for each case and the changes in emissivity depending on the material composition may be a subject of future research. The emissivity of the component is also temperature-dependent, but is assumed to be constant in these simulations. The turbulence model that is used in this thesis is $k-\epsilon$ since it was found to be more stable and not as mesh-dependent as $k-\omega$. For the forced convection case, Scalable Wall Functions wall treatment is used due to independence from the quality of the mesh in comparison to other treatment methods. The Scalable Wall Functions assume fully turbulent flow, so for the natural convection case, Enhanced Wall Treatment is preferred.

Another thing for the external heat transfer is that the forced convection can be simulated with the flow field frozen for more time-efficient calculation. This is also more likely to provide a result less affected by minor changes in the modeling of the fan or the quenched setup, since the actual flow is turbulent and the rate of heat transfer varies remarkably. As can be seen from figure 6.21, the flow collides with the pin near the point where measurements are taken.

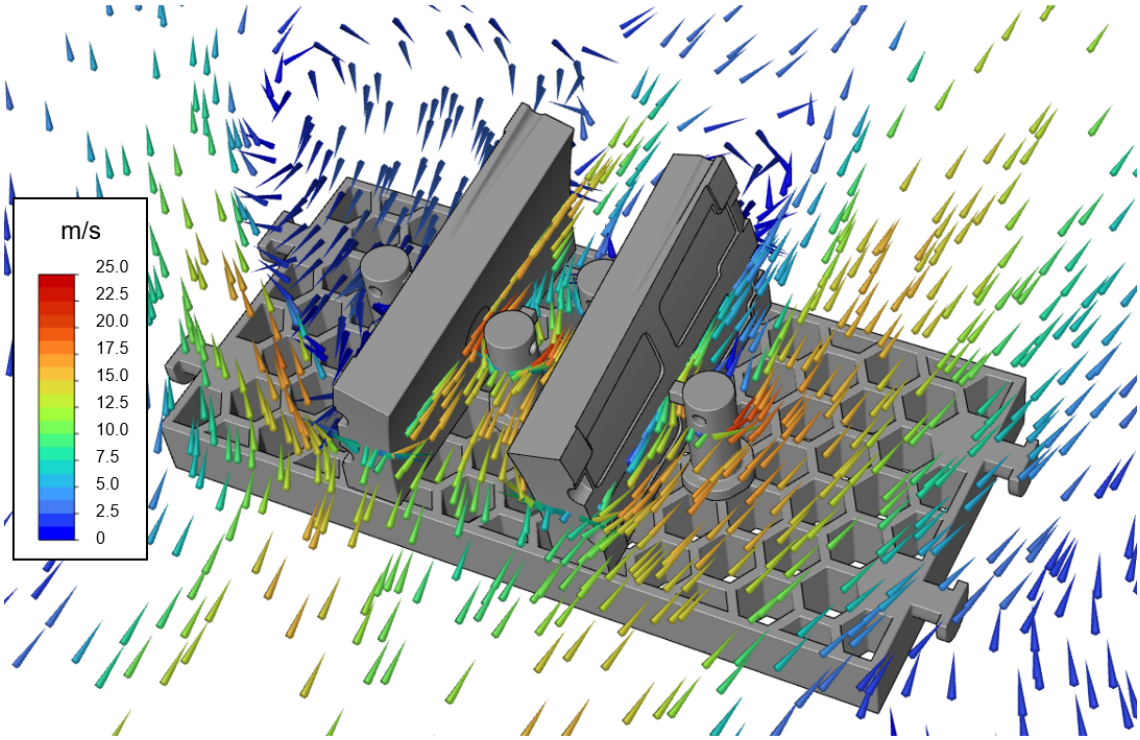

Figure 6.21. *Velocity magnitude in the forced convection case with non-frozen flow field.*

The pin near the measured point disturbs the flow field and causes remarkable variations in the flow pattern near the measured point. Slight differences in geometry and the flow field generated by the fan can have a drastic effect on the cooling rate at the measured

point. As was seen from figure 6.18, the measured point in non-frozen flow does not cool smoothly, the reason of which can be accounted for the disturbed flow near the measured point. Simulating the case with freezing the flow field smooths the cooling curve.

The main contribution of this thesis to the heat transfer simulation of air quenching process was the calculation of phase transformations being correctly implemented in the simulation. As was discussed in section 4.4, most quenching heat transfer simulations described in studies do not take the phase transformations into account. The implementation of the released heat has also been more inaccurate, as was the case with Takeuchi and Yogo (2021). There are still improvements to be made to the heat transfer simulation, such as taking the segregation into account, including temperature dependence of the emissivity and finding a more accurate correlation for the martensitic transformation constant.

7. CONCLUSIONS

This thesis aimed to answer two research questions and carry out one research task. The first research question was about which phenomena have an effect on the air quenching process. The phenomena that are discussed in this thesis are phase transformations occurring in the quenched material and the heat released due to the transformation. Also, the temperature dependence of the thermal conductivity and specific heat are taken into account. The external heat transfer phenomena, radiation and convection, are also discussed in this thesis with the differences between forced and natural convection introduced.

The research task of this thesis was, as stated before, to create a coherent way of simulating cooling of the quenched component while phase changes occur. The phase transformations to bainite and martensite release energy, so the amount of the bainitic and martensitic transformation needed to be calculated each time step so the correct amount of heat would be released. For martensite, this was calculated using the modified Koistinen-Marburger equation 2.10, where the martensitic transformation coefficient was calculated using correlation by Bohemen and Sietsma (2009).

The main achievement of the research task was related to the simulation of the released heat from the phase transformations since this is often ignored in heat transfer simulations of air quenching. An important aspect of this was determining a way to calculate the correct amount of formed bainite since it depends not only on the temperature and the composition of steel, like martensitic transformation, but also on the steel grain size and the time from the beginning of cooling. The equations for calculating this were presented in section 2.2, but implementing these equations to the code was dismissed for being too time-consuming. Instead, the data collected from JMatPro software of phases formed at different constant cooling rates was used and in the simulation, the correct amount of formed bainite was bilinearly interpolated. This way of collecting the data for the bainite formation is not too difficult, as long as the cooling rates are chosen in such a way that the time scale covers the wanted simulation time.

It was also noticed that the JMatPro software estimates the starting temperature of martensitic transformation based on the nominal composition to be lower than it actually is, so using a correlation for the start temperature is advised. In this thesis, the correlation used

was equation 2.9. This and other key factors for modeling air quenching process, that are found in this thesis, are gathered in section 6.7.

The second research question was about evaluating how accurate are the results that can be achieved from the simulation with the chosen way of modeling the process. The cooling rates of the simulations correlated quite well with the measured data in both natural and forced convection cases, and the resulting phase distributions seem realistic. The average error in final natural convection simulation in comparison to measured data was 7.1 % and the root mean squared error 35.8 °C, when the martensitic transformation start temperature was 293.9 °C. The forced convection simulation cooling rate did not improve with increased martensitic start temperature as the natural convection simulation, as can be seen from table 7.1 Both the average and root mean squared error are of the same magnitude in the forced convection simulations compared.

In forced convection simulation, the flow field of the fan is a source of potential inaccuracy. Although some of the uncertainties in fan location and blade inflection point in 3D fan zone model can easily be fixed with more exact data, estimating the pressure jump as constant can also be a cause of slight deviation. Also using a different correlation for martensitic transformation constant could be justified since the slowing effect of the martensitic transformation seems to be initially too steep in both forced and natural convection simulation.

Simulation	average error	root mean squared error (°C)
Frozen flow with M_s 236.8 °C	0.074	24.2
Frozen flow with M_s 293.9 °C	0.079	29.2
Non-frozen flow with M_s 293.9 °C	0.067	32.5

Table 7.1. *Average error and root mean squared error of the forced convection simulation.*

Different ways of modeling a fan and the difference they make to the air quenching process could be a subject of future research, since it is not studied further in this thesis. Another subject of future research could be including temperature-dependent emissivity in simulations since it is assumed to be constant in simulations conducted in this thesis. Composition dependence of the emissivity could also be studied, since it may vary for different steels. A study with the most effect on the accuracy of the simulations could be to investigate whether using different correlation for martensitic transformation constant would improve the accuracy of released heat from martensitic transformation.

REFERENCES

Ansys, Inc. (2023a). *Ansys Fluent Theory Guide*. eng. 23.1. Canonsburg, PA: Ansys Inc.

– (2023b). *Ansys Fluent User's Guide*. eng. 23.1. Canonsburg, PA: Ansys Inc.

ASM handbook. Volume 9, Metallography and microstructures (2004). eng. Materials Park, OH: ASM International. ISBN: 978-1-62708-177-1.

Bohemen, S. M. C. van and J. Sietsma (2009). "Effect of composition on kinetics of athermal martensite formation in plain carbon steels". eng. In: *Materials science and technology* 25.8, pp. 1009–1012. ISSN: 0267-0836.

Bolton, W. (William) (1994 - 1993). *Engineering materials technology*. eng. 2nd ed. Oxford, England: BH Newnes. ISBN: 1-4831-4107-1.

Capdevila, C, F. G Caballero, and C. García de Andrés (2002). "Determination of Ms Temperature in Steels: A Bayesian Neural Network Model". eng. In: *ISIJ international* 42.8, pp. 894–902. ISSN: 0915-1559.

Çengel, Yunus A. (2015). *Heat and mass transfer : fundamentals & applications*. eng. 5. ed. in SI Units. New York: McGraw-Hill. ISBN: 978-981-4595-27-8.

Cheng, Heming et al. (2010). "Determination of Surface Heat Transfer Coefficients of Cr12MoV Steel Cylinder during High-Speed Gas Quenching at Atmospheric Pressure". eng. In: *ASTM Special Technical Publication*. Vol. 1523. 100 Barr Harbor Drive, PO Box C700, West Conshohocken, PA 19428-2959: ASTM International, pp. 84–90. ISBN: 9780803175099.

Churchill, S. W and M Bernstein (1977). "A Correlating Equation for Forced Convection From Gases and Liquids to a Circular Cylinder in Crossflow". eng. In: *Journal of heat transfer* 99.2, pp. 300–306. ISSN: 0022-1481.

Denis, S, D Farias, and A Simon (1992). "Mathematical Model Coupling Phase Transformations and Temperature Evolutions in Steels". eng. In: *ISIJ international* 32.3, pp. 316–325. ISSN: 0915-1559.

Dossett, Jon L. and George E. Totten (Oct. 2014). *Heat Treating of Irons and Steels*. ASM International. ISBN: 978-1-62708-168-9. DOI: 10.31399/asm.hb.v04d.9781627081689. URL: https://doi.org/10.31399/asm.hb.v04d.9781627081689.

Elkatatny, I. et al. (2003). "Numerical analysis and experimental validation of high pressure gas quenching". eng. In: *International journal of thermal sciences* 42.4, pp. 417–423. ISSN: 1290-0729.

Hunkel, M. (2021). In: *HTM Journal of Heat Treatment and Materials* 76.2, pp. 79–104. DOI: doi:10.1515/htm-2020-0006. URL: https://doi.org/10.1515/htm-2020-0006.

Koistinen, D.P. and R.E. Marburger (1959). “A general equation prescribing the extent of the austenite-martensite transformation in pure iron-carbon alloys and plain carbon steels”. In: *Acta Metallurgica* 7.1, pp. 59–60. ISSN: 0001-6160. DOI: https://doi.org/10.1016/0001-6160(59)90170-1. URL: https://www.sciencedirect.com/science/article/pii/0001616059901701.

Lee, Seok-Jae and Young-Kook Lee (2008). “Finite element simulation of quench distortion in a low-alloy steel incorporating transformation kinetics”. eng. In: *Acta materialia* 56.7, pp. 1482–1490. ISSN: 1359-6454.

Li, Yongzhi et al. (2015). “Finite-element Simulation of Low-alloy High Strength Steel Welding Incorporating Improved Martensite Transformation Kinetics and Recrystalization Annealing”. In: *ISIJ International* 55.7, pp. 1448–1453. DOI: 10 . 2355 / isijinternational.55.1448.

Liscic, Bozidar et al. (2010). *Quenching Theory and Technology*. eng. Baton Rouge: CRC Press. ISBN: 9780849392795.

Lusk, Mark and Herng Jou (Feb. 1997). “On the rule of additivity in phase transformation kinetics”. In: *Metallurgical and Materials Transactions A* 28, pp. 287–291. DOI: 10.1007/s11661-997-0131-5.

MacKenzie, D. Scott (2005). “Advances in quenching: A discussion of present and future technologies”. eng. In: *Gear technology* 22.2, pp. 20–26. ISSN: 0743-6858.

Mills, Anthony F. (1999). *Basic heat and mass transfer*. eng. 2nd ed. Upper Saddle River (NJ): Prentice Hall. ISBN: 0-13-096247-3.

Oliveira, Wendell Porto de et al. (2010). “Thermomechanical analysis of steel cylinders quenching using a constitutive model with diffusional and non-diffusional phase transformations”. eng. In: *Mechanics of materials* 42.1, pp. 31–43. ISSN: 0167-6636.

Peet, M.J., H.S. Hasan, and H.K.D.H. Bhadeshia (2011). “Prediction of thermal conductivity of steel”. eng. In: *International journal of heat and mass transfer* 54.11, pp. 2602–2608. ISSN: 0017-9310.

Saunders, Nigel et al. (2004). “The Calculation of TTT and CCT diagrams for General Steels”. In.

Shang, Xiao Feng and Zhi Jian Wang (2010). “Flow and Heat-Transfer Simulation Based on CFD and Experimental Study during High-Pressure Gas Quenching”. eng. In: *Applied Mechanics and Materials* 29-32, pp. 1436–1440. ISSN: 1660-9336.

Takeuchi, Hirohisa and Yasuhiro Yogo (2021). “Jet Quenching Simulation with Consideration for Distribution of Heat Transfer Coefficient and Latent Heat for Martensitic Transformation under Rapid Cooling”. eng. In: *ISIJ international* 61.3, pp. 871–880. ISSN: 0915-1559.

Umakoshi, Y. and H.Y. Yasuda (2011). “Nondestruction Lifetime Prediction by Magnetic Measurements”. eng. In: *Encyclopedia of Materials: Science and Technology*. Elsevier Ltd, pp. 1–9. ISBN: 9780080523583.

Versteeg, H. K. (2007). *An introduction to computational fluid dynamics : the finite volume method*. eng. 2nd ed. Harlow: Pearson/Prentice Hall. ISBN: 978-0-13-127498-3.

Wang, Jing et al. (2008). “Numerical simulation of high pressure gas quenching of H13 steel”. eng. In: *Journal of materials processing technology* 202.1, pp. 188–194. ISSN: 0924-0136.

Wen, Chang-Da (2010). “Investigation of steel emissivity behaviors: Examination of Multi-spectral Radiation Thermometry (MRT) emissivity models”. eng. In: *International journal of heat and mass transfer* 53.9, pp. 2035–2043. ISSN: 0017-9310.

Xu, Zhe-xin et al. (2016). “Numerical simulation on vacuum solution heat treatment and gas quenching process of a low rhenium-containing Ni-based single crystal turbine blade”. eng. In: *China foundry* 13.6, pp. 402–413. ISSN: 1672-6421.